small methods
www.small-methods.com

Synchrotron-Based X-ray Absorption Fine Structures, X-ray Diffraction, and X-ray Microscopy Techniques Applied in the Study of Lithium Secondary Batteries

Weihan Li, Minsi Li, Yongfeng Hu, Jun Lu, Andrew Lushington, Ruying Li, Tianpin Wu, Tsun-Kong Sham,* and Xueliang Sun**

Owing to the recent advance of third-generation synchrotron radiation (SR) sources, SR-based X-ray techniques have been widely applied to study lithium-ion batteries, lithium–sulfur batteries, and lithium–oxygen batteries to solve material challenges. SR-based techniques provide high chemical and physical sensitivity and a comprehensive picture of material structure and reaction mechanisms. An in-depth understanding of batteries is imperative for the development of future energy storage devices with enhanced electrochemical performance to meet societies' growing need for devices with high energy density. Here, recent progress in the application of SR techniques for lithium secondary batteries with a focus on several techniques, including X-ray absorption fine structure, synchrotron X-ray diffraction, and synchrotron X-ray microscopy techniques is reviewed. The working principle for all characterization techniques is introduced to provide context for how the technique is used in the field of energy storage. Through discussing the utilization of SR techniques in different directions of batteries, including electrodes, electrolytes, and interfaces, the practical application strategies of techniques in batteries are clarified. By summarizing and discussing the application of SR techniques in batteries, the aim is to highlight the crucial role of SR characterization in the development of advanced energy materials.

Dr. W. Li, M. Li, A. Lushington, R. Li, Prof. X. Sun
Department of Mechanical and Materials Engineering
University of Western Ontario
London, Ontario N6A 5B9, Canada
E-mail: xsun9@uwo.ca
Dr. W. Li, M. Li, Prof. T.-K. Sham
Department of Chemistry
University of Western Ontario
London, Ontario N6A 5B7, Canada
E-mail: tsham@uwo.ca
Dr. Y. Hu
Canadian Light Source
44 Innovation Boulevard, Saskatoon, Saskatchewan S7N 2V3, Canada
Dr. J. Lu
Chemical Science and Engineering Division
Argonne National Laboratory
9700 South, Cass Avenue, Lemont, IL 60439, USA
Dr. T. Wu
X-ray Science Division
Argonne National Laboratory
9700 South, Cass Avenue, Lemont, IL 60439, USA
E-mail: twu@aps.anl.gov

DOI: 10.1002/smtd.201700341

1. Introduction

Presently, there is a growing demand for energy and as a result has garnered the attention of both the scientific and industrial community. The exploitation of fossil fuels has given rise to serious environmental repercussions, such as global warming and climate change due to emission of harmful greenhouse gasses.[1] This energy and environmental challenge has triggered great interest in the use of renewable and sustainable energy resources, including solar and wind energy.[2,3] Although great progress has been made in the conversion of solar and wind energy into electrical energy,[4,5] the intermittent distribution characteristics of renewable energy sources still limit its practical application. One promising solution is the development of efficient and economic energy storage devices to store the harvested electrical energy. Since its commercialization in 1991, rechargeable lithium-ion batteries (LIBs) have been widely applied in portable electronic devices and have become the dominant energy storage device to power electric vehicles (EVs).[6–8] However, a number of challenges remain for current commercial LIBs to meet the requirements of large-scale energy storage for use in solar and wind energy due to their low energy density and high cost.[9] Beyond LIBs, other lithium-based secondary systems, such as lithium–sulfur (Li–S) and lithium–oxygen (Li–O) have also attracted intensive research attention due to their increased energy density over LIBs.[10–12] However, polysulfide dissolution and oxygen crossover effects (OCE) limit the cyclability and capacity performance of Li–S batteries and Li–O batteries, respectively. Therefore, it is urgent to design and fabricate advanced lithium secondary batteries with enhanced electrochemical performance to meet future global energy market needs.

Based on the working principles, the electrode and electrolyte materials play the central role in the electrochemical performance of lithium secondary batteries.[13] To enable the effective utilization of renewable energy in the future, breakthroughs are required to enhance the energy density and cycling stability of LIBs. This requires an in-depth

understanding of the electrochemical process that occur during cycling as well as reaction and degradation mechanisms associated with electrodes and electrolytes and their interfaces.[14,15] In this regard, various characterization methods have been carried out to probe the electrode and electrolyte materials and their interfaces during cycling. These techniques include scanning electron microscopy (SEM), transmission electron microscopy (TEM), nuclear magnetic resonance (NMR), X-ray diffraction (XRD), X-ray photoelectron spectroscopy (XPS), neutron diffraction, and synchrotron radiation (SR)-based techniques.[16–21] Benefiting from the recent advancements made in the development, third generation SR sources display the highly increased flux and brilliance and broader spectrum (from infrared to hard X-ray) of the X-ray beams, such as Advanced Photon Source and Canadian Light Source, compared to the first and second generation SR sources.[22–24] The great advancement in X-ray beam provides the promising potential to design and develop versatile beamlines and endstations to meet characterization demands without destruction, such as microscopy mapping and in situ or operando study.[14,25] Based on the characterization mechanisms, SR-based X-ray techniques display wide application in LIBs and beyond to investigate the physical and chemical properties of the systems to realize further understanding of electrochemical mechanisms, including X-ray absorption fine structure (XAFS), synchrotron X-ray diffraction (SXRD), and synchrotron X-ray microscopy (SXM) as shown in **Figure 1**.[25–29]

SR-based X-ray techniques are a powerful tool to investigate local physical and chemical properties of materials, such as crystal structure, oxidation state, and local atomic environment. Furthermore, due to the high brilliance, flux, and stability of SR sources, SR-based X-ray techniques provide high energy and structural resolution, allowing for rapid and precise data collection compared to other characterization methods.[25] For instance, XAFS can be tested with two modes, the X-ray absorption near edge structure (XANES) and extended X-ray absorption fine structure (EXAFS), which is highly sensitive to electronic structure and local changes in mateirals.[30] Through the use of in situ XAFS characterization, the electrochemical reaction mechanism of cathode materials for LIBs (e.g., $LiCo_{1/3}Ni_{1/3}Mn_{1/3}O_2$ and $Li_{1.2}Ni_{0.15}Co_{0.1}Mn_{0.55}O_2$) have been investigated by analyzing changes to the electronic and atomic structure of the material.[31,32] During the first charge process (i.e., delithiation), the charge compensation mechanism and capacity contribution has been elucidated through detecting local structural changes. In addition to XAFS, SXM and SXRD have also been widely applied to investigate electrochemical mechanisms, thermal stability, and solid–electrolyte interface (SEI) of LIB electrode materials.[29,31,33–35] Among these two techniques, SXM technique includes transmission X-ray microscopy (TXM), X-ray tomographic microscopy (XTM), X-ray ptychographic microscopy (XPM), and micro-X-ray fluorescence (μ-XRF) spectroscopy based on the working principles. SR-based X-ray techniques provide researchers with an opportunity to comprehensively understand electrochemical process and their related influence factors, in order to advance optimization and design of battery electrodes and

Tianpin Wu is the principle beamline scientist working at beamline 9-BM of the Advanced Photon Source, Argonne National Laboratory. Her expertise is in energy storage and catalyst materials characterization by X-ray absorption spectroscopy. She received her undergraduate degree in chemistry from the University of Science and Technology of China, and her Ph.D. degree in physical and analytical chemistry from the University of Utah. Following two and half years of postdoctoral research in the Division of Chemical Sciences and Engineering at Argonne National Laboratory, she joined the X-ray Science Division as a physicist in 2012.

Tsun-Kong Sham is a Distinguished University Professor and a Canada Research Chair in Materials and Synchrotron Radiation at the University of Western Ontario. He obtained his Ph.D. from the University of Western Ontario (1975) with a B.Sc. from the Chinese University of Hong Kong. He joined the Chemistry Department at Brookhaven National Laboratory in 1977 and returned to Western in 1988. He is presently the Director of the Soochow-Western Center for Synchrotron Radiation, a Fellow of the Royal Society of Canada and an Officer of the Order of Canada. His expertise lies in nanomaterial synthesis, surface and interface, X-ray absorption related spectroscopy, and microscopy. His recently focus is nanostructure phase transition, assembly of nanocomposites, in situ/ operando studies of energy materials and devices. X-ray excited optical luminescence in the energy and time domain, nanomaterials for drug delivery, and micro-beam analysis of cultural and heritage materials.

Xueliang (Andy) Sun is a Canada Research Chair in Development of Nanomaterials for Clean Energy, Fellow of the Royal Society of Canada and Canadian Academy of Engineering and Full Professor at the University of Western Ontario, Canada. He received his Ph.D. in materials chemistry in 1999 at the University of Manchester, UK, which he followed up by working as a postdoctoral fellow at the University of British Columbia, Canada and as a Research Associate at L'Institut National de la Recherche Scientifique (INRS), Canada. His current research interests are associated with advanced materials for electrochemical energy storage and conversion, including electrocatalysis in fuel cells and electrodes in lithium-ion batteries and metal–air batteries.

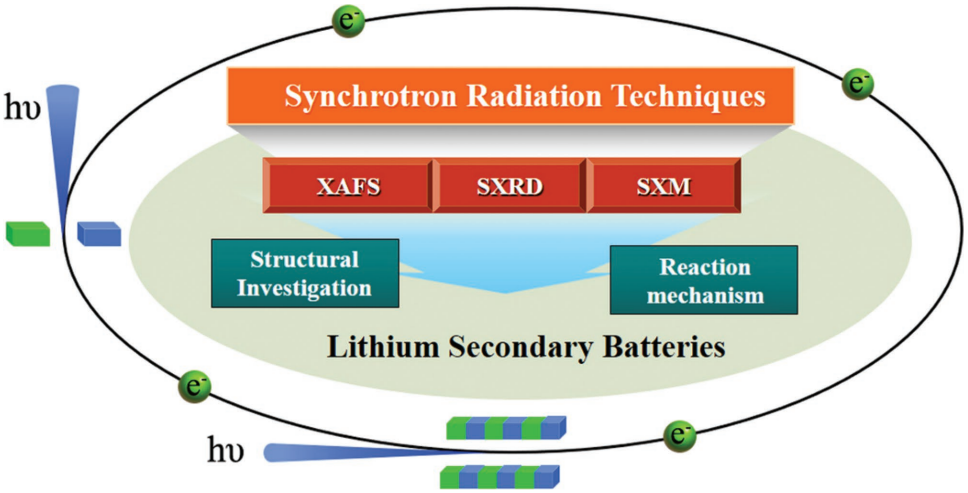

Figure 1. Schematic illustration of the origin of synchrotron radiation and representative SR techniques applied for lithium secondary batteries to probe the structure and reaction mechanism.

electrolyte and further improve electrochemical performance. Here, we summarize the recent progress in advanced SR-based X-ray techniques characterization for LIBs with an emphasis on application of different techniques for various research purposes, including XAFS, SXRD, and SXM.

2. X-ray Absorption Fine Structure and Applications

XAFS is a powerful technique that is used to study the local structure around active atoms at the atomic and molecular scale. The technique is rooted in observing oscillations in the X-ray absorption coefficient energy near and above the binding energy of the element in question.[36] The physical principles of XAFS rely on principles laid out in the photoelectric effect and use the interaction between outgoing and scattered photoelectron wavefunctions to determine. XAFS can be measured in three modes, transmission, fluorescence yield (FLY), and total electron yield (TEY). Using these three different detection mechanisms, information at various depths can be extracted. XAFS in transmission mode is designed to probe the flux intensity of X-ray beams before and after being transmitted through the sample, and is used to reveal the overall information of the transmitted samples. TEY mode is more surface sensitive with up to around several nanometers probing depth, while FLY mode can provide information at deeper probing depths of approximately several hundreds of nanometers and give information about the bulk of the material.[37–41]

Based on the energy range, the XAFS spectra can be divided to two regions, XANES and EXAFS.[42,43] XANES is sensitive to oxidation state and coordination environment of the element in question. Information is often obtained by analyzing the position and shape of the absorption edge.[44–47] On the other hand, EXAFS spectra are typically used to determine the local structure of the active atom and can provide information pertaining to nearest neighbor, coordination number and species of neighboring atoms. In order to extract this information, the EXAFS equation is used and best fits are assigned.[48–50] In addition, elemental specificity and atomic sensitivity make XAFS available for not only crystalline materials but also amorphous and disordered materials. Therefore, XAFS is suitable for studying changes in electrode and electrolyte materials during electrochemical processes.[51] In this section, we will introduce the application of XAFS for battery materials focusing on the study of structural investigation and electrochemical reaction and degradation mechanisms.

2.1. Structural Investigation

2.1.1. X-ray Absorption Near Edge Structure

Since the electronic structure and local chemistry environment (e.g., symmetry and ligand boding environment) of active elements in electrodes and electrolyte play a key role in the charge and discharge process of lithium secondary batteries, XANES has been widely developed as a tool to study numerous electrode and electrolyte materials.[46,52–56] In addition, to improve the electrochemical performance of lithium secondary batteries, several strategies have been carried out to modify electrochemical materials, such as ball milling,[55] applying the use of coating layers,[57,58] doping of heteroatoms,[59,60] and fabrication of bonding structures.[61–64] XANES can also be used to probe changes to the electronic structure and local environment following structural modification.

The valence states of elements in electrode and electrolyte materials determine the electrochemical activity during cycling. For electrode and electrolyte materials, the valence states of pristine materials play a crucial role in predicting the electrochemical reaction and/or degradation mechanism during cycling. In addition, modification strategies may further complicate the valence states of elements. Therefore, the study and investigation of valence states in electrochemical materials becomes of paramount importance. XANES has been widely carried out to service this issue.

Layered lithium transition metal (e.g., Ni, Co, Mn, and so on) oxide composites, such as $LiNi_{1/3}Co_{1/3}Mn_{1/3}O_2$ (NCM) and $LiNi_{0.8}Co_{0.15}Al_{0.05}O_2$ (NCA), have been intensively studied

as promising cathode materials for LIBs due to their high capacity and low cost.[65,66] However, cation mixing between lithium and transition metal ions and capacity fading limit the understanding and application of NCM for large-scale energy storage devices and EVs. To investigate the electronic structure of NCM, Ceder and co-workers[52] clarified the valence states in NCM through the use of XANES. By comparing the XANES of elements in NCM and reference material, XANES was able to identify Ni, Co, and Mn in NCM to have the valence states of +2, +3, and +4, respectively. In this regard, the reaction mechanism of NCM can be predicted to be based on Ni^{2+}/Ni^{4+} and Co^{3+}/Co^{4+} redox reactions. The importance of this finding will be discussed in detail in Section 2.2.1. In addition to confirming the valence states of elements in pristine materials, XANES has also been widely applied to probe changes in chemical states of electrode and electrolyte materials after modification which is aimed at altering the structure in an effort to improve electrochemical performance. In the case of NMC, lithium substitution in the transition metal layers has been intensively studied to obtain increased capacity (i.e., above 280 $mAhg^{-1}$), and is coined as Li-rich NMC or high-energy NMC (HENMC).[65] However, HENMC usually suffers from several interface issues, including oxidization of the electrolyte and serious transition metal dissolution into the electrolyte, leading to short lifetime and safety issues. In this regard, surface chemistry methods are able to restrain interfacial reactions from occurring between the electrolyte and electrodes through the use of a coating layer on the surface of the electrode. As shown in **Figure 2**, Xiao et al.[57] designed and prepared $AlPO_4$ (AP)-coated HENMC (HENMC-AP) via atomic layer deposition (ALD) to overcome the challenges faced with using HENMC. Through comparing the electrochemical performance of HENMC-AP with different thickness of $AlPO_4$, the obtained electrode materials with 20 ALD-cycles, denoted as HENMC-20AP, displayed improved cyclability and Coulombic efficiency (CE). The mechanism accounting for the improved electrochemical performance was studied using XANES. As displayed in Figure 2A,B, to obtain the valence state of Co before and after the ALD process, spectra of the Co $L_{3,2}$-edge XANES were obtained and fitted alongside a linear combination of standards such as CoO and $LiCoO_2$. Comparing the fitting results reveals a decrease of Co^{3+} amount and an increase in Co^{2+} following ALD of $AlPO_4$. As the Co $L_{3,2}$-edge XANES spectra are recorded using surface-sensitive TEY mode, the result suggests that the surface of HENMC is reduced during the ALD process. The reduction process also applies to elemental Mn, as shown in Figure 2C. Combined with the HRTEM results, displayed in Figure 2D, the surface of HENMC is confirmed to be reduced to a spinel phase due to the ALD process, allowing for faster ion migration during cycling. The XANES spectra show good resolution in testing valence states of elements and is a powerful technique to probe the electronic structure of elements in materials.

In addition to elemental electronic structure, local chemical environment, such as symmetry, ligand, and bonding states, will also affect the electrochemical performance of electrode and electrolyte materials. Therefore, identifying the local chemical environment will lead to a better understanding of electrochemical reactions. Since it is difficult to obtain information pertaining to the local chemical environment through traditional characterization techniques (e.g., SEM, TEM, and XPS), XANES analysis provides the possibility of exploring the local chemical environment.

In the case of solid-state electrolytes (SSE) for LIBs, ligand structure affects the lithium-ion diffusion of the material and will influence lithium-ion conductivity.[67] Therefore, information regarding ligand structure can impart crucial knowledge for understanding ion transportation mechanism, and can be investigated using XANES.[53] Wang et al. prepared lithium silicate (LSO) SSE thin films via ALD and studied the oxygen ligand environment through the use of Si K-edge XANES spectra. By comparing the XANES spectra of LSO and standard samples (i.e., Na_2SiO_3, quartz, and nanosized SiO_2), Si in the

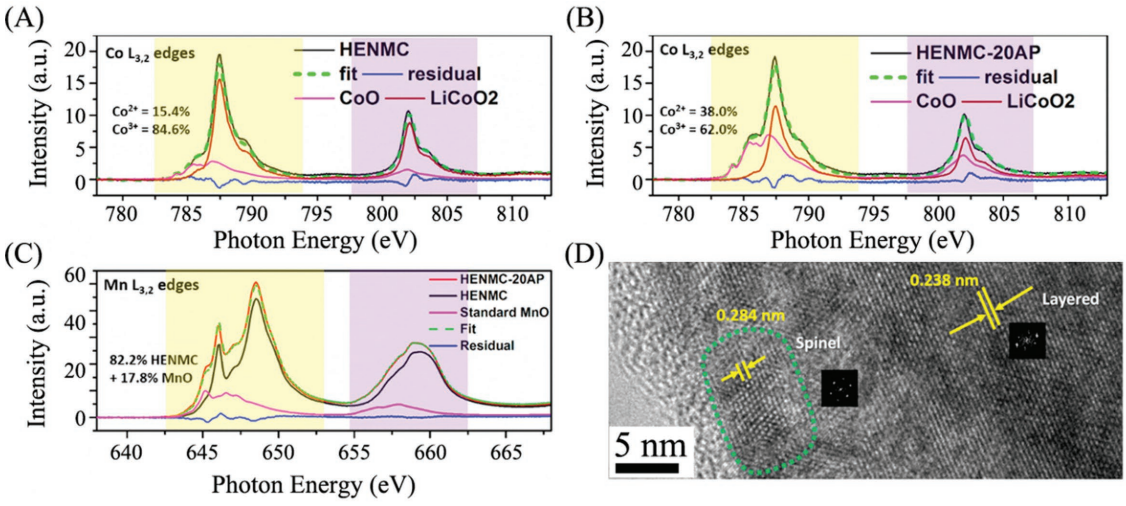

Figure 2. Co $L_{3,2}$-edge XANES spectra of: A) HENMC and B) HENMC-20AP. Both the spectra are fitted to standard CoO and $LiCoO_2$. C) Mn $L_{3,2}$-edge XANES of HENMC and HENMC-20AP. The XANES spectra of HENMC-20AP is fitted to the HENMC and standard MnO. All the XANES spectra are recorded by the TEY mode. D) HRTEM image of HENMC-20AP. The inset shows the fast Fourier transform patterns. Reproduced with permission.[57] Copyright 2017, Elsevier.

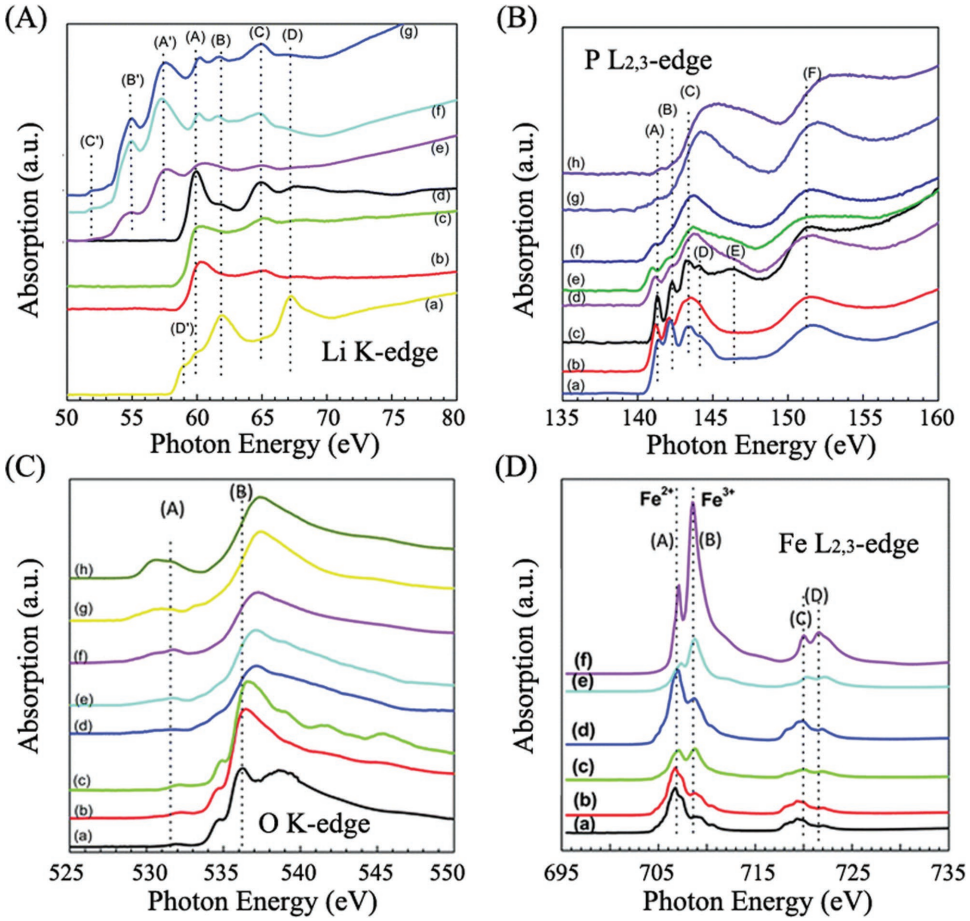

Figure 3. A) Li K-edge XANES spectra of the Li containing compounds: (a) Li_2CO_3, (b) $LiPO_3$, (c) $Li_4P_2O_7$, (d) Li_3PO_4, (e) amorphous $LiFePO_4$, (f) disordered $LiFePO_4$, and (g) crystalline $LiFePO_4$. B) P $L_{2,3}$-edge XANES spectra of the P containing compounds: (a) $LiPO_3$, (b) $Li_4P_2O_7$, (c) Li_3PO_4, (d) crystalline $LiFePO_4$, (e) disordered $LiFePO_4$, (f) amorphous $LiFePO_4$, (g) $Fe_3(PO_4)_2$, and (h) $FePO_4$. C) O K-edge XANES spectra of the oxygen containing compounds: (a) $LiPO_3$, (b) $Li_4P_2O_7$, (c) Li_3PO_4, (d) crystalline $LiFePO_4$, (e) disordered $LiFePO_4$, (f) amorphous $LiFePO_4$, (g) $Fe_3(PO_4)_2$, and (h) $FePO_4$. D) Fe $L_{3,2}$-edge XANES spectra of Fe-containing compounds: (a) crystalline $LiFePO_4$, (b) disordered $LiFePO_4$, (c) amorphous $LiFePO_4$, (d) $Fe_3(PO_4)_2$, (e) $FePO_4$, and (f) Fe_2O_3. All the XANES spectra are recorded by the FLY mode. Reproduced with permission.[46] Copyright 2012, Royal Society of Chemistry.

LSO thin films was found to exist in a tetrahedral oxygen ligand environment. Furthermore, through a combination of surface-sensitive TEY and bulk-sensitive FLY modes, a similar ligand structure was observed at both the surface and in the bulk of LSO thin films. In addition to ligand structure, due to the effect on the unoccupied electronic states, symmetry and neighboring atoms have a crucial influence on the electronic states of atoms in materials,. However, it is difficult to obtain information via traditional characterization methods, especially with regards to proving chemical environments with elements in multiple valence states. XANES is a useful technique that can be used to identify elements with different local chemical structures.[46] As displayed in **Figure 3**, Yang et al. displayed Li K-edge, P $L_{2,3}$-edge, O K-edge, and Fe $L_{3,2}$-edge XANES spectra of different elements-containing compounds, which are related to the preparation and electrochemical reaction process of $LiFePO_4$. By using this fingerprint method, in-depth information regarding chemical environment can be obtained. XANES spectra have the promising potential of identifying and quantifying the synthesis and charge/discharge process of $LiFePO_4$-based electrode materials. Hence, it is rational to apply this XANES method to probe elements with alternate chemical environments in other electrode and electrolyte materials.[68,69]

In addition to the study of chemical environments, the bonding structure of composite electrode materials is another crucial factor that will influence the electrochemical performance of batteries. It is usual to form bonding structure to bind electrochemically active materials to the substrates, such as Si-carbon nanotubes,[70] Sn-graphene,[62] SnO_2-graphene,[61,63,71] $LiFePO_4$-graphene,[64] and Se-carbon nanofibers composites.[72] As shown by Zhou et al.,[71] the C K-edge XANES spectra display an obvious increase in intensity following binding to SnO_2. In addition, the bonding structure can also lead to a shift in the edge threshold position, with new peaks and shape changes occurring to the C K-edge XANES spectra due to electron donation from SnO_2, as reported by Wang et al.[63] XANES provides powerful evidence to confirm the formation of bonding structures in composite materials and can improve the design and preparation of electrode materials aimed at achieving enhanced electrochemical performance.

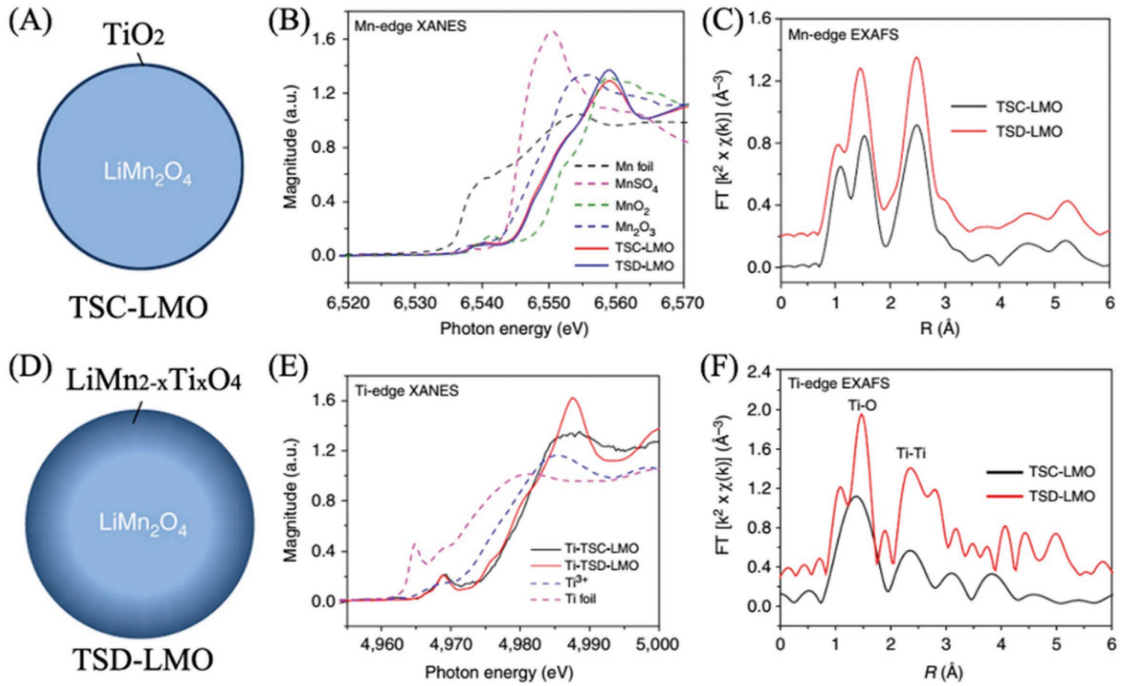

Figure 4. Schematic illustration of: A) TSC-LMO and D) TSD-LMO. B) Mn K-edge XANES, C) Mn K-edge EXAFS, E) Ti K-edge XANES, and F) Ti K-edge EXAFS spectra of TSC-LMO (k = 2–7.5 Å^{-1}) and TSD-LMO (k = 1.7–12 Å^{-1}). Reproduced with permission.[58] Copyright 2014, Nature Publishing Group.

2.1.2. Extended X-ray Absorption Fine Structure

While the XANES spectra can provide information regarding electronic structure and local chemical environment, the EXAFS spectra are primarily used to determine information about local lattice structure, including distances, coordination number, and neighboring atom species, and to study lattice distortion and phase changes within a material.[73–75] Since local lattice structure plays an important role in determining ion/e$^-$ diffusion, phase composition, and electrochemical reaction mechanism, it is crucial to probe this aspect of the material in order to achieve and further improve electrode and electrolyte materials.

EXAFS analysis can not only elucidate the lattice structure (e.g., coordination environment) of electrode materials,[31,76–79] but also predict and confirm the lattice structure and phase composition of unknown electrode materials that are often used for LIBs and Li–O batteries.[58,80,81] As shown in **Figure 4**, Lu et al.[58] used EXAFS to determine the effect of surface-doping in $LiMn_2O_4$ cathode materials, a process which demonstrated improvement to cyclability of the material. Different from the ALD process of preparing an amorphous TiO_2 layer on the surface of $LiMn_2O_4$ particles (TSC-LMO), a TiO-surface-doped $LiMn_2O_4$ (TSD-LMO) was prepared using a sol-gel method. The Mn K-edge XANES and EXAFS and Ti K-edge XANES spectra indicated that the valence state of Ti on the surface and in the bulk is identical. However, two extra bonding peaks were observed in the Ti K-edge EXAFS of TSD-LMO and suggests diffusion of Ti^{4+} into the surface of LMO and the formation of surface-doped $LiMn_{2-x}Ti_xO_4$ layers. This example highlights the use of EXAFS in determining local lattice structure and phase composition of materials with multiple valence states in different regions of electrochemical materials. In addition to the investigation of lattice structure, lattice distortion is another key factor that can affect the electrochemical activity of materials. Among them, Jahn–Teller (JT) distortions are a major cause for concern and result in structural instability and capacity fading in many cathode materials used for LIBs, including spinel and layered lithium transition metal oxides.[82–85] As the EXAFS spectra are very sensitive to interatomic distance and coordination number, it is rational to use this technique to probe JT transitions in electrode materials.[86–89] $LiMn_2O_4$ is one typical spinel cathode material used in LIBs and suffers from JT distortions induced by Mn^{3+} situated at octahedral sites and results in detrimental structural instability.[90–92] Yamaguchi et al.[86] studied the effect of JT distortion transitions in $LiMn_2O_4$ at various temperatures by extracting the coordination number and interatomic distance from EXAFS spectra, which investigated the phase transition of $LiMn_2O_4$ at different temperature. At low temperatures (around 200 K), the JT distortion of Mn^{3+} is cooperative and leads to macroscopic distortions in the material. However, at elevated temperatures (around 300 K), the JT effect was found to be local and induce noncooperative distortion in $Mn^{3+}O_6$ octahedra structures within the material. Observation of noncooperative JT distortions has also been reported for layered $LiNiO_2$ cathode material.[88,89] Two main strategies have been applied to suppress JT distortions in $LiMn_2O_4$, including replacing Mn^{3+} with JT-inactive elements,[82,93] and reducing particle size to diminish effects related to volume change.[94,95]

As XANES and EXAFS are suitable for tracking changes to local electronic and chemical structures of materials, the use of XAFS can provide complimentary information of electrode and electrolyte materials for lithium secondary batteries. Based on the fundamental structural information of electrode and

electrolyte materials, the electrochemical mechanism can be analyzed and the challenges facing the electrochemical applications can be clarified. Then the rational modification strategies based on the fundamental investigation will be carried out to improve the electrochemical performance.

2.2. Electrochemical Reaction and Degradation Mechanism

As discussed in Section 2.1, the electronic structure and local chemical and lattice environment will affect the electrochemical process. However, it is really difficult to predict the electrochemical reaction and even degradation mechanism based on the original structure information of materials. On the other hand, it is possible to probe the mechanism via combining electrochemical reaction and degradation process with XAFS characterization strategies. During electrochemical cycling, valence states as well as the local geometric environment undergo changes due to the diffusion of lithium and other elements in the material. Based on this theoretical prediction, lithium secondary batteries have been intensively studied with the use of XAFS to find out what happens during the process, including electrochemical reaction,[96–99] formation of interfaces between electrodes and electrolytes.[34,100–104] In this section, the study of electrochemical reactions as well as degradation mechanisms of lithium secondary batteries will be introduced and summarized with a focus on the application of XAFS.

In order to track the structural and phase evolution of lithium secondary batteries through XAFS, several techniques have been developed up to now, mainly including ex situ, in situ, and operando studies. During the ex situ XAFS study, the electrochemical systems stop at desired states, like different potential or capacity during cycling. Then the interesting sections in the systems would be analyzed by XAFS by disassembling batteries. In the case of in situ or operando XAFS studies, the materials in the batteries will be directly tested by XAFS at desired states without disassembling. There are slight differences between in situ and operando studies. While the in situ study is going to analyze materials in batteries stopped at desired states, the operando study needs special cells, which is in operation during XAFS measurement.[105–107] Compared to the in situ and operando studies, the ex situ XAFS study displays high signal-to-noise (S/N) ratio and resolution due to less signal influence from battery cases and other noninteresting materials in the batteries. However, the battery disassembling process in the ex situ XAFS study would make the possible metastable state and oxygen/moisture-sensitive samples at risk and cannot get very accurate information. The in situ and operando studies can avoid the possible risks resulted from the battery disassembling and are preferred to get better understanding of battery systems. Nevertheless, the in situ or operando cell design and development are main challenges for the measurement and have the lower S/N ratio problem. Therefore, the ex situ study can be the best choice if the samples can keep off from the risks. Fortunately, plenty of in situ and operando XAFS studies have been realized and provide further understanding of lithium secondary batteries.

2.2.1. Electrochemical Reaction Mechanism

The study of electrochemical reaction mechanisms for electrode materials used in lithium secondary batteries lies on the investigation of electronic structure and local environment of electrodes during the lithiation and delithiation process. Preliminary investigations on chemically deintercalated electrode materials were conducted using XANES and EXAFS to study the delithiation process in LIBs.[77,108] Shortly after, ex situ XAFS characterization strategies, combined with electrochemical charge and discharge were carried out to directly analyze the electrochemical process.[97,109–113] Although ex situ XAFS can provide static information of electrodes at states of equilibrium during the electrochemical process, dynamic electrochemical behavior is unattainable through ex situ experiments. Therefore, in situ and operando XAFS was developed to attain a more holistic understanding of the electrochemical reactions taking place during battery cycling. In this regard, the development of cells for in situ and operando characterizations is crucial but provides an avenue in creating a powerful tool to probe electrochemical reactions in real time.[106,114–116]

The key point for the mechanism study is to confirm the active element sites of electrode materials during cycling. Numerous reports have applied the use of ex situ XANES and EXAFS to study transition elements and oxygen of cathode materials for LIBs during cycling. As shown in **Figure 5**, Qiao et al.[111] measured the Ni $L_{3,2}$-edge and Mn $L_{3,2}$ edge XANES spectra of $LiNi_{0.5}Mn_{1.5}O_4$ electrodes at different states of charge (SOC) to confirm the active sites during electrochemical cycling. For this study, the XANES spectra were used to investigate the valence states of elements during cycling by analyzing the threshold energy position and shape with the calculated XANES spectra of Ni^{2+}, Ni^{3+}, and Ni^{4+}. Their investigation determined that Mn is electrochemically inactive during cycling and has no valence. The active element during cycling was found to be Ni with a two-phase redox reaction (i.e., Ni^{2+}/Ni^{3+} and Ni^{3+}/Ni^{4+}) involved during the charge compensation mechanism. Additionally, alternate reaction mechanisms between the surface and bulk of the electrode material have also been investigated by carrying out surface-sensitive TEY and bulk-sensitive FLY detection. The Ni^{2+} phase on the electrode surface was confirmed to be electrochemically inactive, contrary to Ni^{2+} in the bulk of the material. Based on the study of valence state change of electrochemically active elements during cycling, the ligand environment change after cycles can also be studied via XANES spectra. Hy et al.[117] measured XANES spectra of $Li_{1.2}Ni_{0.2}Mn_{0.6}O_2$ after cycles and displayed evidence for the migration of Ni from octahedral to tetrahedral sites. In addition to elucidating the function of transition metal elements in the cathode materials for LIBs, XANES analysis can also provide information regarding the participation of elemental oxygen during electrochemical cycling of $LiCoO_2$ cathode material.[118] The absorption peak shoulder in the O K-edge XANES spectra during delithiation provides evidence for the existence of oxygen in a higher oxidation state. In addition to XANES spectra, EXAFS analysis has also been widely applied to track the change of crystal structures and structural instability during cycling, which is related to the degradation mechanism after cycles. Kim and Yo[119]

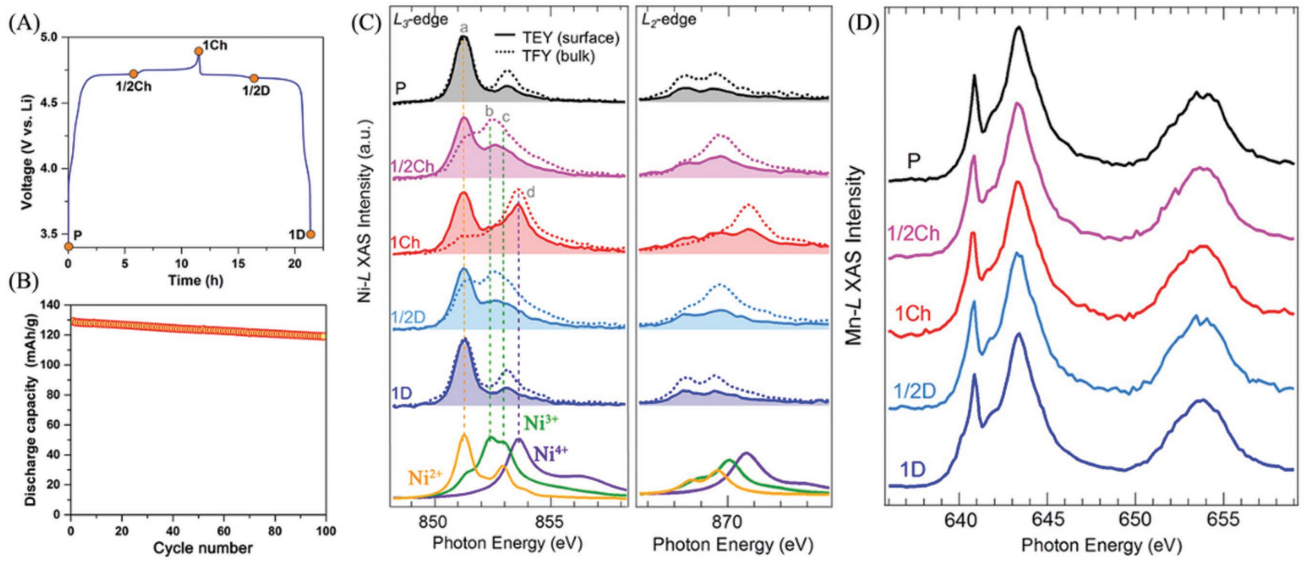

Figure 5. A) Voltage profiles of $LiNi_{0.5}Mn_{1.5}O_4$ cathode during the initial charge/discharge cycling. The ex situ XAS study was performed at different states (marked with orange dots): pristine electrode (P), 50% charge state (1/2Ch), 100% charge state (1Ch), 50% discharge state (1/2D), and 100% discharge state (1D). B) Capacity retention of $LiNi_{0.5}Mn_{1.5}O_4$ cycled at 0.1 C rate. C) Ni L_3- and L_2-FLY and TEY XANES spectra of $LiNi_{0.5}Mn_{1.5}O_4$ at different states as shown in (A). The calculated spectra of Ni^{2+}, Ni^{3+}, and Ni^{4+} were done in an octahedral crystal field. Reproduced with permission.[111] Copyright 2015, American Chemical Society.

studied the change in interatomic distance and structure distortions for $LiCo_{0.85}Al_{0.15}O_2$ during delithiation with the use of EXAFS. As elucidated by the k-space and R-space spectra obtained from EXAFS analysis, all bond pairs showed decrease in interatomic distance and the crystal structure displayed increase in distortion with the increased Debye–Waller factor. The obvious change of local structures can be the main reason for the capacity degradation in the following cycles. In addition to the ex situ XAFS study of overall electrode materials during cycling, ex situ XANES imaging techniques provide the chance to track the electrochemical reaction in different regions of electrode materials. Katayama et al.[120] used the XANES imaging of $LiFePO_4$ cathode to obtain the chemical state maps for the electrodes at different discharge and charge states, which can provide the evidence of lithium diffusion in electrode materials during cycling. In principle, it is difficult to track elemental lithium by X-ray techniques as the very low binding energy. Several groups applied SR X-ray techniques to track the evolution of other elements related to the lithium, such as elemental Fe and P in $LiFePO_4$, to reflect the distribution and diffusion of lithium during cycling.[120–123] Based on the report of Katayama et al., the reaction distribution of the $LiFePO_4$ electrodes is inhomogeneous and the reason is the different resistance in different parts of electrodes, which is related to the migration of lithium ion and electron. In the case of lithium ion, the migration in the electrolyte–electrode interfaces and electrode particles will lead to different resistance.

In addition to ex situ XAFS characterization, in situ XAFS characterization has also been carried out to study the electrochemical reactions and dynamics of LIB electrode materials in real time.[48,51,78,120,124–126] Yoon el al.[50] utilized in situ XAFS to track the valence change of electrochemically active elements and changes to the crystal structure of $LiNi_{0.5}Mn_{0.5}O_2$ during the first charge and discharge process. By tracking the shape of the Ni K-edge and Mn K-edge XANES spectra during the first cycle, a two-step redox reaction of elemental Ni (i.e., Ni^{2+}/Ni^{3+} and Ni^{3+}/Ni^{4+}) was determined. However, during the first discharge process, at a lower region of ≈1 V, only the reduction of Mn^{4+} was found to account for the charge compensation without involving a Ni redox reaction. Furthermore, in situ EXAFS provided evidence of possible distortions in the local structure during the first charge process, mainly due to replacement of lithium with metal ions in the Ni^{2+}/Mn^{4+} layer. Later, Yoon et al.[32] and Tsai et al.[96] studied NMC cathode materials using in situ XAFS. The active elements for charge compensation mechanism are confirmed to be Ni and O. Moreover, in situ EXAFS not only show the change of Ni—O bond length due to oxidization of Ni^{2+} but also provides information about structure distortion during the charge and discharge process. Since the Ni^{3+} is JT effect active site, the structure distortion is confirmed by the change of Debye–Waller factor, resulting in change of bond length. In the study by Yoon et al.[32] and Tsai et al.,[96] studying charge compensation mechanism of NMC, the Mn and Co were considered as electrochemically inactive sites. Although the threshold energy position does not show a distinct shift in the Mn K-edge and Co K-edge XANES spectra, the spectra still demonstrate a drastic change in shape. Since the shape of the XANES spectra is highly sensitive to the local structure, the change to spectra's shape should be further analyzed. As shown in **Figure 6**, Yu et al.[31] applied in situ XANES and EXAFS to study the Ni, Mn, Co K-edge during the first charge process of Li-rich layered $Li_{1.2}Ni_{0.15}Co_{0.1}Mn_{0.55}O_2$. Similar to the results observed for NMC, as discussed above, the Ni K-edge XANES spectra display a continuous shift in the threshold energy position to higher energy ones, indicating

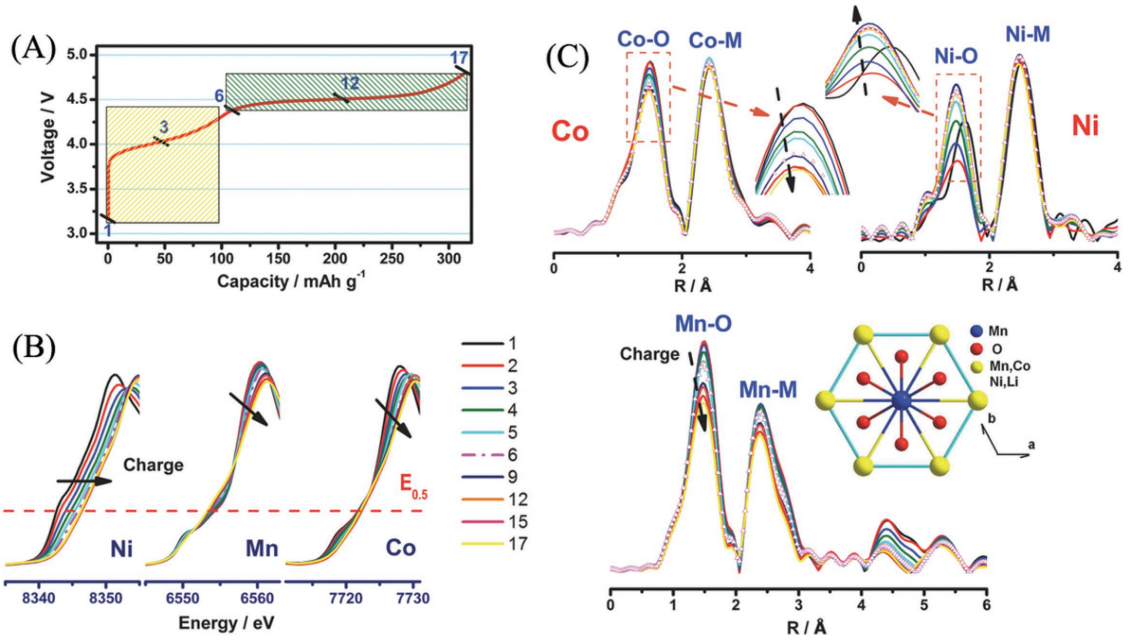

Figure 6. A) The voltage profile of $Li_{1.2}Ni_{0.15}Co_{0.1}Mn_{0.55}O_2$ during the first charge process with the current density of 21 mAg^{-1}. Selected XAS scan numbers are marked on the charge curve. B) Normalized Ni, Mn, and Co K-edge spectra and C) magnitude of the Fourier transformed Mn, Co, and Ni K-edge spectra of $Li_{1.2}Ni_{0.15}Co_{0.1}Mn_{0.55}O_2$ during the first charge process. The inset shows a schematic illustration of the coordination environment around the transition metal ions. Reproduced with permission.[31] Copyright 2014, Wiley-VCH.

that the oxidization of Ni^{2+} to Ni^{4+} during the first charge process. Although the threshold energy position of the Mn and Co K-edge spectra maintains the same position during the delithiation process, the shape of the XANES spectra and the Fourier transformed (FT) EXAFS spectra shows obvious changes in the Co-O and Mn-O peak intensity. The FT EXAFS spectra suggest that the participation of elemental Mn and Co in the charge compensation during delithiation and the varied change tendency in different charge states investigate that the elemental Co and Mn are mostly related to the voltage slope and voltage plateau regions, respectively. Through further analyzing the Debye–Waller factors, changes to the local environment around Mn also suggest structure distortions related to Mn, which can be the main reason for the capacity fading with prolonged cycling. Using in situ XAFS, the charge compensation mechanism in Li-rich layered $Li_{1.2}Ni_{0.15}Co_{0.1}Mn_{0.55}O_2$ has been confirmed and found to be different from NMC. Study of the electrochemical mechanism can give rise to a better understanding of the electrochemical process and aid in the development and preparation of advanced electrode materials.

In the case of Li–S batteries, the insulating nature of sulfur and the detrimental effect of the polysulfides shuttle effect are the two main challenges for the practical application and commercialization of this promising technology.[12,127,128] To overcome these issues, it is urgent to investigate and understand the sulfur redox reaction. Cuisinier et al.[99] utilized operando XANES spectra of the S K-edge to track formation and changes to sulfur-related phases in Li–S batteries during cycling. The operando spectra were analyzed by using standard S_8, S_6^{2-}, S_4^{2-}, and S^{2-} spectra as the reference spectra to linearly fit the result. During the charge process, the sulfur redox reaction undergoes step-by-step process with shorter chains sulfur (i.e., S_4^{2-} and then S_6^{2-}) and final oxidization of S_6^{2-} to S_8. The discharge process also shows a stepwise reaction while the discharge capacity is mostly limited by unreacted sulfur and not the presence of insoluble Li_2S_2. The investigation of different charge and discharge processes can explain the hysteresis between the two events. A further understanding of the sulfur redox reaction is crucial for the design of advanced Li–S batteries and improve their electrochemical performance. In addition to the application of Li–S batteries at room temperature, an extended electrochemical window for the operation of Li–S batteries is required to meet practical applications requirements for EVs. Since current ether-based electrolytes for Li–S batteries cannot operate at high temperatures, the utilization of carbonate-based electrolytes should be one potential solution for extending the electrochemical operation window. However, side reactions between carbonate-based electrolytes and polysulfides lead to rapid consumption of electrolyte and capacity degradation. To solve this issue, the reaction mechanism of carbonate solvents should be further studied and a valid solution should be determined. As shown in **Figure 7**A, Xiao and co-workers[129] first studied the electrochemical process of Li–S batteries with carbonate-based electrolytes via ex situ XANES spectra and reported the observance of new peaks in the spectra belonging to side reactions occurring between polysulfides and the carbonate solvent. To overcome this side reaction, an alucone coating was deposited on the surface of C–S electrodes via molecular layer deposition. Utilizing this coating layer, the occurrence of side reactions was found to be suppressed. The investigation of Li–S batteries with different electrolytes and modification strategies by XAFS can provide valuable information in understanding and addressing other challenges currently faced in the field of Li–S batteries.

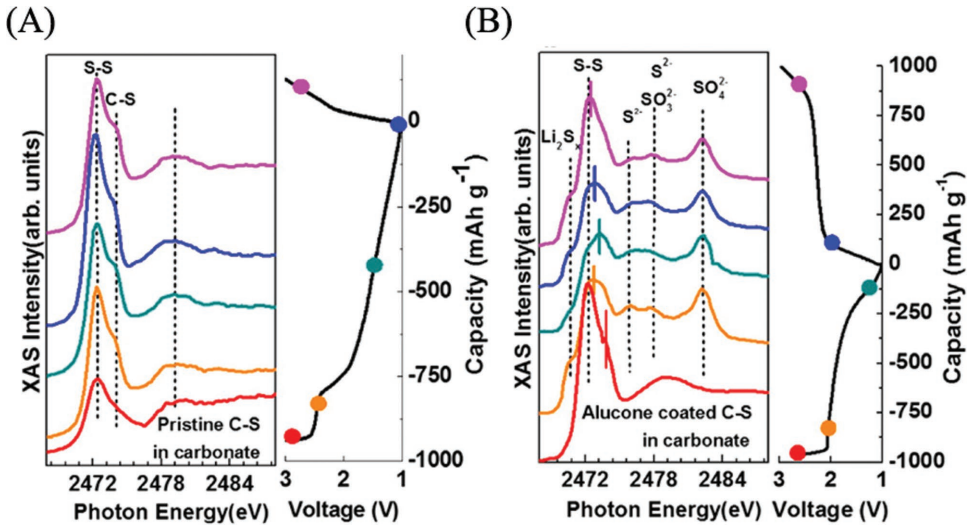

Figure 7. Sulfur K-edge spectra of: A) C-S electrodes and B) alucone-coated C–S electrodes with carbonate-based electrolyte at discharge–charge steps. Reproduced with permission.[129] Copyright 2016, American Chemical Society.

2.2.2. Interface Study

As the passivation interlayer between electrodes and electrolyte for LIBs, the SEI plays a key factor in stabilizing the electrode and electrolyte during cycling. Investigation of the SEI during cycling can lead to a comprehensive understanding of its formation and evolution and help to design stable SEIs for electrodes and electrolytes in LIBs. LiF has been confirmed to be a major component of the SEI through the collection of F K-edge XANES spectra of the surface of electrode materials, due to decomposition of $LiPF_6$.[34,130] Additionally, the SEI is confirmed to be formed during the first discharge and charge process. Qiao et al.[101] reported a more detailed study of the SEI at different crystal planes of Sn via measuring F, O, and C K-edge XANES and determined that the components of the SEI are primarily LiF and Li_2CO_3 and from due to electrolyte decomposition. However, which crystal plane is exposed will affect the composition of the formed SEI on Li_2CO_3 with LiF being the main composition on Sn (100) and (001) surfaces, respectively. Furthermore, the effective passivation of LiF has been confirmed to prevent decomposition of electrolyte while the Li_2CO_3 layer shows continuous growth and consumption of electrolyte. In this regard, the formation of LiF as a primary component of the SEI is essential for stable electrochemical performance of LIBs. The XAFS spectra provide a powerful monitoring strategy to study the evolution of SEI of designed electrode materials and contribute to the decision about what structure and composition are rational to form stable SEI and realize highly improved electrochemical performance.

On the other hand, the electrolyte can also have a crucial influence on the solid–liquid interface at electrode materials prior to electrochemical reaction. By using total-reflection fluorescence XAFS (TRF-XAFS), Takamatsu et al.[102] and Yamamoto et al.[131] studied the electronic structure of electrode/electrolyte interface of $LiCoO_2$ and $LiFePO_4$ in LIBs after immersion into carbonate electrolyte. Through two detection modes (TEY and FLY), elemental Co at the surface of $LiCoO_2$ was determined to be reduced by the electrolyte with negligible influence on elemental Co in the bulk of $LiCoO_2$ and $LiFePO_4$. The reduction of Co at the surface results in an initial degradation to the capacity. Moreover, Co and Ni $L_{3,2}$-edge XANES spectra of $LiNi_{0.8}Co_{0.15}Al_{0.05}O_2$ also confirm the reduction of elements in electrodes materials following electrolyte contact and results in a cationic disordered phase near the surface and seriously impedes charge transfer.[104] As the side reaction at the interface can be probed by XAFS, related challenges can be overcome by coating with a passivation layer prior to contact with the electrolyte.

3. Synchrotron X-ray Diffraction

XRD is a powerful technique to determine crystallographic information of crystalline materials, including cell parameters, strain, and microstructural information and has been widely applied in lithium secondary batteries.[132,133] Based on different working principles, there are three typical X-ray diffraction techniques, including X-ray powder and single-crystal diffraction and X-ray Laue diffraction. While the first two techniques use monochromatic X-ray, the last one can apply polychromatic X-ray to test materials combined with 2D detectors.[134–136] Compared with the laboratory XRD, SXRD shows higher brilliance and flux and tunable energies of X-ray beam due to the synchrotron resource, which can strengthen the intensity of signals and shorten testing time. The high intensity of SR X-ray beam flux makes SXRD suitable for microprobe characterization (X-ray microdiffraction) to track microstructure of electrode or electrode materials evolution during cycling.[122,137,138] Additionally, owing to the large range of tunable energies of SR X-ray beams, energy-dispersive X-ray diffraction (EDXRD) has been intensively developed to probe the different sections of electrode materials with the ability to penetrating the testing batteries with metal cases.[121,139,140] SXRD can provide a high level of structural detail and time resolution for electrode and electrolyte materials. As discussed in the XAFS section, the structural investigation of lithium secondary batteries plays a crucial role in studying electrochemical reaction mechanisms and stability.

In situ and operando SXRD has been intensively carried out to study the electrochemical reaction mechanism of insertion, conversion, and alloy-type electrode materials with a focus on tracking structural and phase evolution and the formation of defects and strain in lithium-ion,[141–149] Li–S/Se,[28,98,150,151] and Li–O_2[152–154] batteries with cycling and operation at various temperatures.

3.1. Electrochemical Reaction in LIBs

In the case of LIBs, Thurston el al.[155] showed an early attempt in the investigation of structural changes during cycling via SXRD at 1996. Through measuring the SXRD patterns of electrode materials at different discharge states, lattice parameters changes during the electrochemical reaction were studied. Shortly after, several electrode materials were studied using in situ/operando SXRD technique to track the lattice parameters and phase variation during the cycling, showing the evidence of the electrochemical reaction mechanism, such as layered and spinel oxides.[144,156,157]

Based on the collection of real-time electrochemical cycling data, intermediate phases were found to form during cycling reaction. While monoclinic Li-rich Li_yVO_2 phase has been found to be formed during the cycling of VO_2, some solid-solution intermediates have been confirmed during the electrochemical reaction $LiNi_{0.5}Mn_{1.5}O_4$.[143,158] In addition to the investigation of stable intermediates during electrochemical cycling, time-resolution SXRD (TR-SXRD) was used to capture and track metastable phases formed during the cycling process.[159–162] As shown in **Figure 8**, Orikasa et al.[161] studied the formation of nonequilibrium intermediate phases during phase transitions between $LiFePO_4$ (LFP) and $FePO_4$ (FP) via TR-SXRD. A single new diffraction peak was observed during the cycling process, indicating the formation of an intermediate phase. The intermediate phase was then confirmed to be metastable due to the disappearance of this new peak during the relaxation process following electrochemical cycling. Furthermore, the calculated lattice constant values based on the SXRD patterns suggest that the metastable intermediate phase is a Li_xFePO_4 (x = 0.6–0.75) solid-solution phase. Moreover, the formation of a metastable intermediate phase during cycling would contribute to the high rate performance of Li_xFePO_4.[160,161] In addition to the electrochemical mechanism study of LFP through SXRD, microprobe SXRD can also be used to track the reaction distribution of LFP during cycling. Additionally, the lithium distribution and diffusion in electrode materials can be analyzed through tracking the distribution of LFP and FP.[122,123] Strobridge et al.[123] applied in situ microprobe energy-dispersive X-ray diffraction to track the electrochemical reaction in LFP during cycling and confirmed the inhomogeneous distribution in electrodes. Through analyzing the distribution of LFP and FP in the electrodes in the coin cells, the lithium distribution can also be studied. Along with the electron migration in electrodes, the lithium diffusion in electrolyte and electrode can control the reaction distribution. The higher current densities would break the uniformity of reaction and lead to inhomogeneous distribution. By providing a detailed electrochemical reaction mechanism, SXRD can also be utilized to determine the reason for the energy decay of electrode materials by tracking variations in structure during electrochemical cycling. Through elucidating the variation in lattice parameter during and after cycling, irreversible changes to the structure are considered as the main reasons for capacity decay in $Li_{1.2}Ni_{0.15}Co_{0.1}Mn_{0.55}O_2$.[31] Additionally, the irreversible variation in microstrains could also lead to the voltage decay of $Li_2Ru_{0.75}Ti_{0.25}O_3$.[142]

3.2. Electrochemical Reactions in Li–S and Li–O Batteries

Owing to excellent resolution of structure for electrode materials, SXRD has become a valuable characterization strategy for investigating complicated redox reactions involved in Li–S and Li–O batteries. For instance, Tan et al.[150] prepared a Li_2S@graphene composite as an electrode material for Li–S batteries and reported the use of in situ SXRD to study the sulfur redox reaction. As shown in **Figure 9**, the intensity of the diffraction peaks for Li_2S displayed a gradual decrease with the appearance of S_8 phases during the initial charge process, indicating a phase transition from Li_2S to S_8. Afterward, the S_8 phase was determined to be consumed quickly accompanied with the formation of Li_2S during discharging. However, no obvious diffraction peaks appeared to be related to Li_2S, indicating the amorphous characteristic of the formed Li_2S at a fully

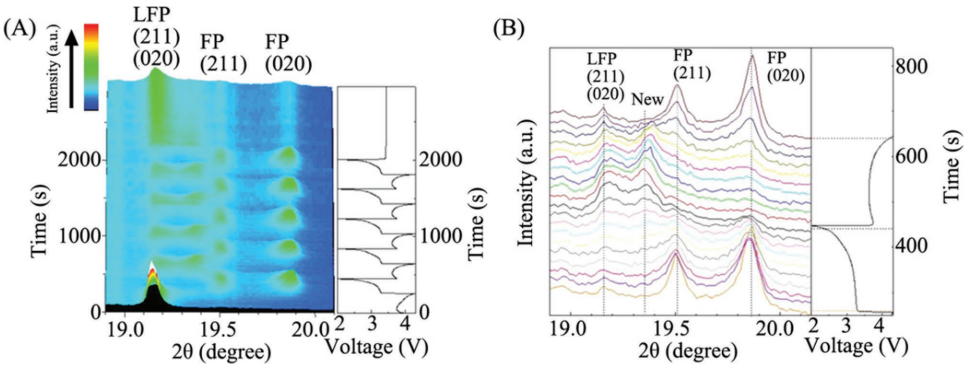

Figure 8. A) Time-resolved SXRD patterns for Li_xFePO4 during cycling at the current density of 10 C. B) Detailed SXRD patterns during the first discharge and second charge reactions. The voltage profiles are displayed at the right. Reproduced with permission.[161] Copyright 2013, American Chemical Society.

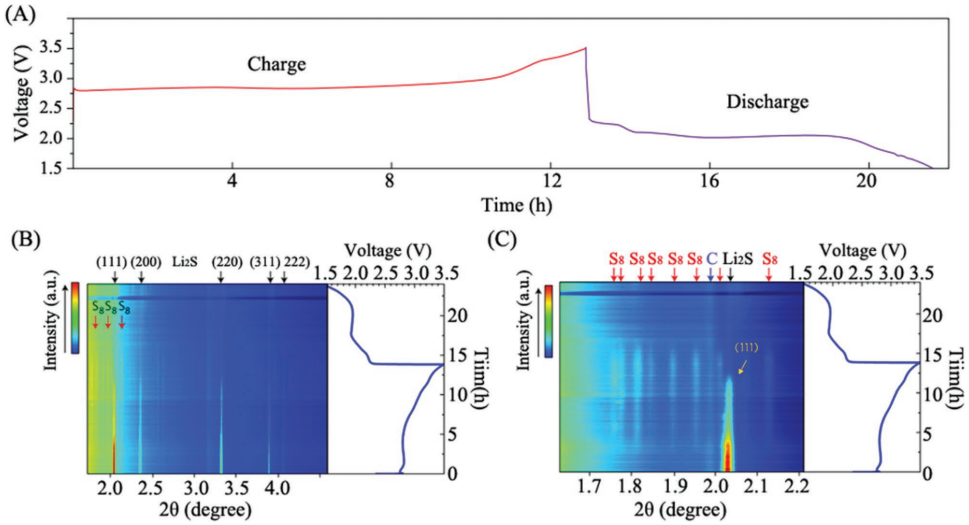

Figure 9. A) Initial charge–discharge voltage profiles of Li_2S@graphene electrode. B) In situ SXRD pattern and C) its enlarged plot of the Li_2S@graphene electrode during the initial charge–discharge process. The black, red, and blue arrows reveal the diffraction peaks of L_2S, S_8, and graphene, respectively. Reproduced with permission.[150] Copyright 2017, Nature Publishing Group.

discharged state. However, these results are contrary to ex situ diffraction results, where crystal Li_2S was detected following lithium intercalation.[28] Nelson et al. compared the results from operando and ex situ SXRD information and demonstrated that crystallized Li_2S might be related to the post-treatment of samples. The results reveal the significant importance of in situ SXRD for dynamic study of electrochemical processes. The use of in situ and operando SXRD characterization strategies is capable of providing accurate information and can further the understanding of Li–S batteries and accelerate the development of advanced Li–S batteries with high energy density.

Similar to Li–S batteries, Li–O batteries demonstrate a high theoretical energy density but suffer a myriad of difficulties such as the oxygen crossover effect (OCE), decomposition of electrolytes, and slow kinetics.[11,163] To determine the root of these issues, it is crucial to understand the electrochemical reaction mechanism and formation of byproducts (e.g., LiOH and Li_2CO_3). Benefiting from in situ/operando SXRD characterization, significant progress has been made in the investigation of the mentioned reaction mechanism.[152–154] Ryan et al.[152] utilized in situ SXRD to confirm the reversible formation of Li_2O_2 on air electrodes with a variation in particle size during the discharge process, indicating a two-stage growth process with primary and secondary nucleation sites. In addition, the lithium anode has also been investigated via the microfocused SXRD (μ-SXRD).[153] It was demonstrated that side reaction at the lithium anode would convert Li to non-electrochemically active LiOH during the electrochemical process. The side reaction was predicted to be a result of ether-based electrolyte decomposition, resulting in the production of H_2O at the cathodes during discharge and charge. Continuous decomposition of the electrolyte and consumption of lithium were found to lead to rapid capacity fade and eventual cell failure. The further understanding of the Li–O battery system requires intensive investigation, including development of lithium anode and electrolytes to improve structural stability and cyclability.

3.3. Thermal Instability of Electrodes for LIBs

In addition to the electrochemical performance of electrode materials for LIBs, safety issues, especially ones related to thermal abuse, are another major barrier to the practical applications of this promising technology.[164–166] In this regard, the thermal stability of electrode materials plays a crucial role in the overall thermal safety of LIBs. The operation of these cells at elevated temperatures could lead to phase changes and decomposition of electrode materials with conditions deteriorating at discharged and charged states. The thermal instability of electrode materials needs valid solutions to prevent possible resulted battery failures and dangerous thermal runaway. Therefore, the systematic study of thermal instability is urgently required to obtain a comprehensive understanding of potential hazards.

In the case of cathode materials for LIBs, delithiated states usually present thermal instability, while the fully lithiated states are generally considered to be thermally stable.[167–169] Several reports present the study of thermal instability of delithiated cathode materials via use of in situ SXRD. As shown in **Figure 10**, Nam et al.[29] utilized in situ TR-SXRD to track phase changes in $Li_{0.33}Ni_{0.8}Co_{0.15}Al_{0.05}O_2$ ($Li_{0.33}$NCA) and $Li_{0.33}Ni_{1/3}Co_{1/3}Mn_{1/3}O_2$ ($Li_{0.33}$NCM) without contacting electrolyte during heating. Phase changes can be recorded by observing changes in peak intensity of specific phases. The two overcharged electrode materials showed different thermal instability, with $Li_{0.33}$NCM displaying enhanced thermal endurance compared to $Li_{0.33}$NCA. By ramping up the temperature from ambient conditions to about 460 °C, $Li_{0.33}$NCA was found to undergo change from rhombohedral to spinel and finally to a rock salt phase. However, for $Li_{0.33}$NCM, the temperature for phase transition from spinel to rock salt was found to be much higher due to the existence of a Co_3O_4 spinel structure in $Li_{0.33}$NCM when heated above 400 °C. Apart from the influence of structure and composition on thermal stability, exposed chemical environment was also found to effect thermal

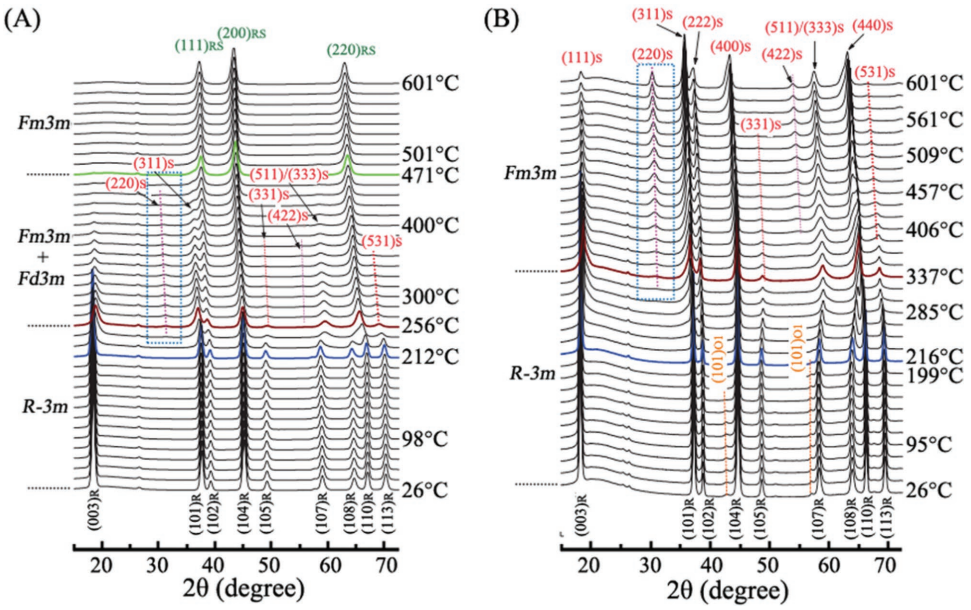

Figure 10. TR-SXRD patterns of the overcharged A) $Li_{0.33}Ni_{0.8}Co_{0.15}Al_{0.05}O_2$ and B) $Li_{0.33}Ni_{1/3}Co_{1/3}Mn_{1/3}O_2$ during the heating process from room temperature. The heating rate is 2.4 °C min^{-1}. The subscripts R, S, and RS denote rhombohedral, spinel, and rock salt structure, respectively. The subscript O1 represents CdI2-type MO2 (M = Ni, Co, and Mn) structure. Reproduced with permission.[29] Copyright 2013, Wiley-VCH.

stability. Chen et al.[170,171] studied the effect of electrolyte components on the thermal instability of $Li_{1-x}(Ni_{1/3}Co_{1/3}Mn_{1/3})_{0.9}O_2$ and $Li_{1.2-x}Ni_{0.15}Mn_{0.55}Co_{0.1}O_2$ via in situ SXRD. Variations in the SXRD pattern during the heating process confirmed the negative effect of organic electrolyte solvent on electrode materials, providing electrons to facilitate the decomposition of electrode materials. Interestingly, $LiPF_6$ salt presents a different function on the thermal decomposition reaction in the two materials. $LiPF_6$ can lead to the formation of MnF_2 on the surface of $Li_{1.2-x}Ni_{0.15}Mn_{0.55}Co_{0.1}O_2$, which can shield the active electrode and slow down thermal decomposition. However, for $Li_{1-x}(Ni_{1/3}Co_{1/3}Mn_{1/3})_{0.9}O_2$, $LiPF_6$ was found to accelerate decomposition and is rooted in a proton intercalation mechanism. Benefiting from in situ SXRD characterization, the understanding of thermal reactions in cathode materials for LIBs becomes deeper and comprehensive. A better understanding of the thermal failure mechanism is crucial to the rational design of electrode materials, in favor of enhancing thermal safety of LIBs.

3.4. Surface Microstructure of Solid-State Electrolytes for LIBs

In addition to tracking the electrochemical reaction distribution in electrode materials through X-ray microdiffraction, X-ray Laue microdiffraction has also been used to study the effect of surface microstructure on solid-state electrolytes for LIBs by tracking the grain orientation direction and grain boundaries distribution.[172] Due to the increasing demand of high safety and energy density of LIBs, SSEs have attracted intense research attention to replace liquid-based electrolytes. However, the low ionic conductivity is the main challenge for the solid-state batteries.[173–175] As the prepared SSE is always ceramic electrolytes with polycrystalline and plenty of grain boundaries, the impedance and lithium diffusion will be affected by the microstructure of SSE. It is urgent to find out how the grain boundary structure affects the electrochemical performance. Cheng et al.[172] carried out the X-ray Laue microdiffraction of garnet phase Al-substituted $Li_7La_3Zr_2O_{12}$ (LLZO) solid-state electrolytes to study the effect of grain boundary structures on the ionic conductivity. As shown in **Figure 11**, the grain orientation and misorientations of neighboring grains in LLZO samples with large and small grains have been studied, showing similar surface structure. By comparison, the higher ionic conductivity of LLZO with small grains can be attributed to the larger amount of surface layer grain boundaries and the grain orientation and grain boundary misorientation effects show no major influence on ionic conductivity.

4. X-ray Microscopy

The XAFS and SXRD techniques discussed above have been intensively developed to obtain structural and composition information of electrode and electrolyte materials for lithium secondary batteries, showing wide-spread application. In principle, the acquired spectra usually provide average information for the samples tested and heterogeneous composition of the material cannot be tracked. However, the heterogeneous characteristics of electrode materials, especially during the cycling, have been demonstrated as the main origin accounting for the complicated behaviors of materials, including cracking, failure, and instability.[176] Hence, structural and compositional investigation at the nano- and microscale is of great importance to probe the heterogeneities of materials and mechanisms that are shielded by characterization techniques that only provide averages. The characterization at this length scale can be provided

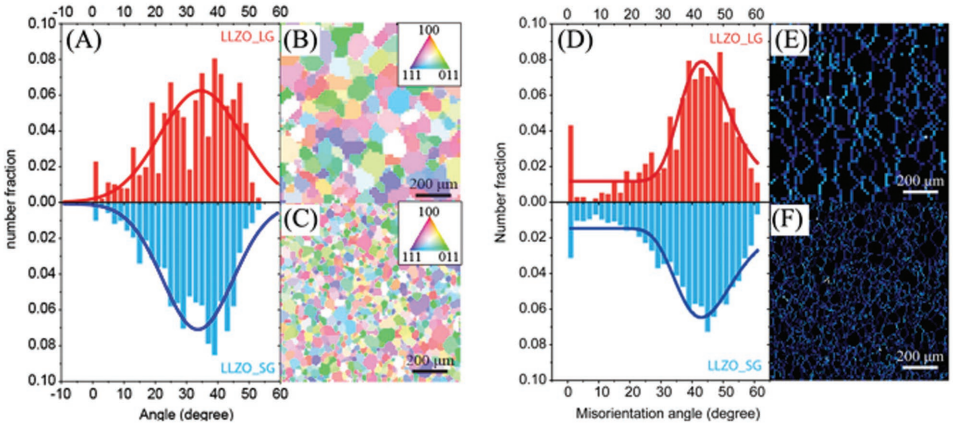

Figure 11. A) Histograms of angles between grain orientation (100) direction and sample plane normal for LLZO with large grains (top) and LLZO with small grains (bottom). Grain orientation mapping of B) LLZO with large grains and C) LLZO with small grains. D) Histograms of misorientation angles of LLZO with large grains (top) and LLZO with small grains (bottom). E) Misorientation angle mapping of LLZO with large grains. Reproduced with permission.[172] Copyright 2015, American Chemical Society.

by several techniques, such as SEM, TEM, and SXM.[177] Considering the working principles, several SXM techniques have been applied in the study of lithium secondary batteries, such as TXM, XTM, XPM, and μ-XRF spectroscopy. The application of X-ray microscopy techniques for LIBs and Li–S batteries will be summarized and discussed in this section with a focus on TXM and XTM.

4.1. Transmission X-ray Microscopy

TXM is analogous to visible light bright-field microscopy, probing the morphology of samples illuminated with quasi-monochromatic X-rays. Morphological investigation is achieved by recording the intensity of transmitted X-rays to reflect the different attenuation coefficient of specific areas in the sample.[176] Since the attenuation of specific elements is related to X-ray energy and shows elemental characteristics near the X-ray absorption edge, the distribution of specific elements can be investigated via TXM. Furthermore, based on the characterization strategies, TXM can be carried out in two modes, that is, full filed (FF-TXM) and scanning (STXM) mode. FF-TXM is achieved by focusing transmitted X-rays with the use of an objective zone plate lens. This is different from STXM which applies focused incident beam through zone plates to probe one small spot at one time. This difference provides FF-TXM and STXM with a unique technical advantage in performing X-ray microscopy in less time and can be done using a lower dose of radiation. Both techniques are capable of probing samples at the nanoscale and provide similar morphological information. Benefiting from the modified imaging configuration and through the use of beam-focusing equipment, a resolution of 20 nm and below can be achieved by TXM.[178] Furthermore, TXM is usually performed in combination with other synchrotron techniques, such as fluorescence yield[179] and XAFS[180] to obtain structural and chemical information simultaneously. The features of TXM make it suitable and rational to probe heterogeneities in lithium secondary batteries.

FF-TXM and STXM have been intensively applied to probe structural changes in electrode materials during cycling of cathode and anode materials for LIBs and Li–S batteries.[28,181–183] For instance, Nelson et al.[28] utilized FF-TXM to track the structure variation of a sulfur/super P composite particles during lithium intercalation and deintercalation, as shown in **Figure 12**. During the discharge process, particles underwent a slight expansion and the dissolution of polysulfide resulted in a more porous structure and an increase in the absorption efficiency of the background around the particle. Furthermore, a comparison of the sulfur intensity in the particle and the background and structural changes during the following charge process suggest that the formed polysulfide during the discharge process was primarily trapped in the super P matrix. However, a small amount of dissolved polysulfide can lead to rapid capacity fading. TXM provides direct evidence of structural variations in electrode materials during electrochemical cycling and provides essential information in the study of reaction mechanisms.

Since the structural variation information of electrode materials acquired from TXM and STXM is not enough to provide a holistic picture of the electrochemical reaction, it is required to get the further phase and chemical information of the various parts of electrode materials during cycling. As discussed above, XANES analysis is a powerful technique to accurately probe the electronic structure and local chemical environment. XANES has been combined with TXM to elucidate variations in phase and chemical states and morphology evolution of electrode materials during electrochemical reaction simultaneously.[177,180] However, the acquisition mechanisms of XANES spectra for FF-TXM and STXM are different based on the technical principles. In the case of STXM, a series of XANES spectra are obtained via scanning energy across the X-ray absorption edge of the interested elements point by point to form the spectra mapping.[184] As for FF-TXM, a series of TXM images are initially recorded as a sequence of X-ray photon energies across the absorption edge. Then changes to the TXM intensity at each pixel or point, as a function the photon energy, can be used as the XANES spectra.[180,185] In spite of

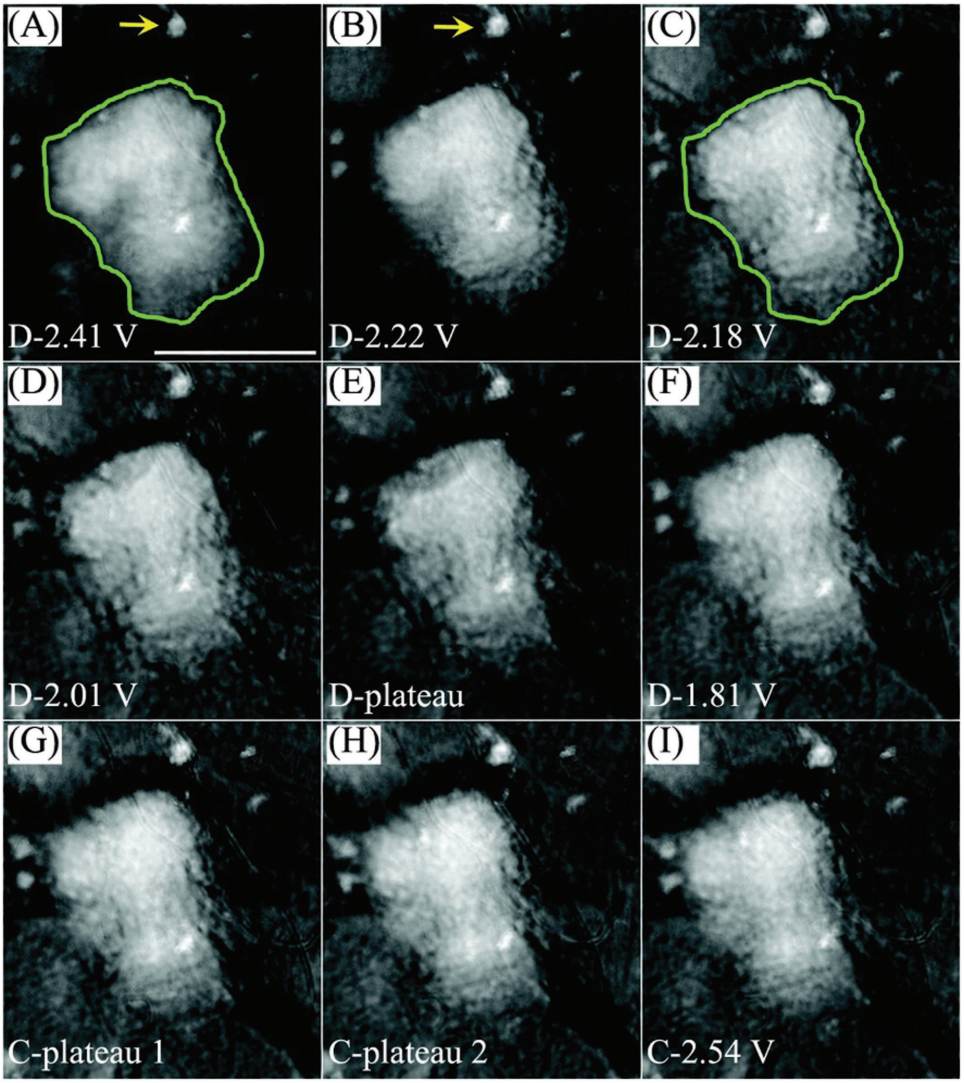

Figure 12. A–I) Operando TXM images of a sulfur/super P composite particle during operation, where the letters "D" and "C" correspond to the discharge and charge states at different voltage values and the voltage plateau states. Images are taken at 6 keV. The brighter section indicates more sulfur throughout the thickness. The green outline around the particle in (A) is replicated in (C) to show the change in particle size and porosity. The scale bar is 10 µm. Reproduced with permission.[28] Copyright 2012, American Chemical Society.

the different realization strategies of FF-TXM-XANES and STXM-XANES, the two techniques show a similar capability in providing chemical and morphological information with similar spatial resolution. Furthermore, by analyzing a series of XANES spectra at different points with a reference spectrum of standard samples, chemical and phase state mapping of the electrode can be obtained.

$LiFePO_4$ as a promising cathode material for LIBs and has been intensively studied with the use of TXM-XANES to give a comprehensive picture of phase transformations during cycling.[33,183,186–188] As discussed in the SXRD section, a metastable intermediate phase was determined to form during the phase transition of $LiFePO_4$ at high charging rates and is not observed at lower charging rates.[161] Hence, the phase transition behavior of $LiFePO_4$ is suggested to be rate-dependent. Wang et al.[33] carried out FF-TXM-XANES imaging to track the phase transition of $LiFePO_4$ at low and high charging rates. As shown in **Figure 13**, a mapping of the phase state is acquired by fitting a XANES spectra at various points of charge alongside reference XANES spectra for $LiFePO_4$ and $FePO_4$. By comparing the mapped phase transition, a clear rate-dependent mechanism is observed for $LiFePO_4$. While $LiFePO_4$ particles undergo a concurrent transition with homogeneous phase distribution at a low rate, two coexist phases are observed during the phase transition at elevated charging rates. In addition to the single particle, the phase transition behavior of many-particle $LiFePO_4$ electrode was also found to be rate-dependent. Chueh et al.[187,188] studied the effect of charging rate on the intercalation of $LiFePO_4$ particles in phase transition by STXM-XANES. The many-particle electrode displayed particle-by-particle-like phase transitions at low rates, but more concurrent transition behavior was observed at a higher charge rates. Additionally, Boesenberg et al.[183] utilized FF-TXM-XANES to track the phase and morphology evolution of $LiFePO_4$ during

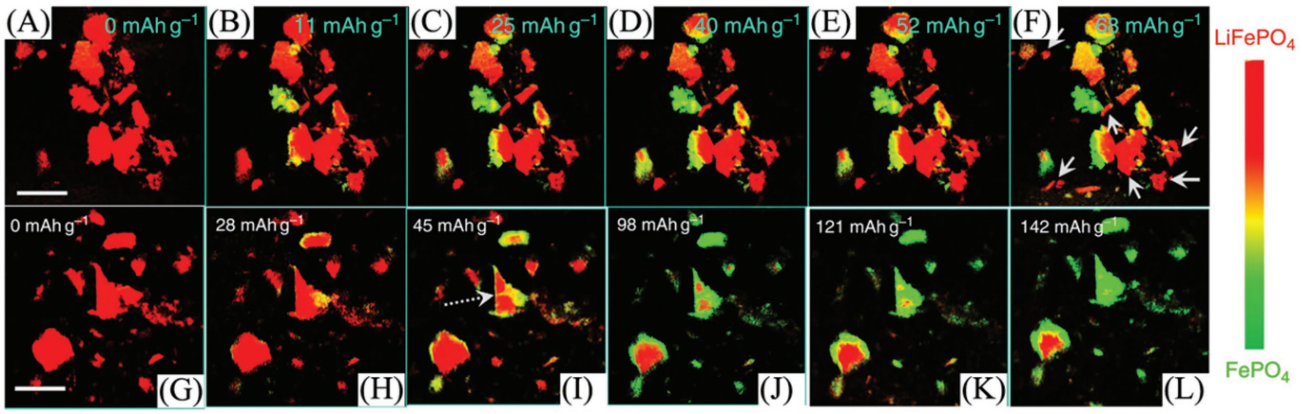

Figure 13. Temporal phase transition of $LiFePO_4$ at: A–F) a high charging rate of 1C, and G–L) a low charging rate of 0.02C. The phase mapping is acquired by linearly fitting XANES spectra of each pixel with $LiFePO_4$ and $FePO_4$ reference spectra at different charged states. The scale bar is 10 µm. Reproduced with permission.[33] Copyright 2014, Nature Publishing Group.

lithium deintercalation and showed that a heterogeneous phase transition can induce cracks in the electrode material. A heterogeneous phase transition and induced cracking of other electrode materials, including NMC and $LiMn_2O_4$, has also been studied using FF-TXM-XANES,[189,190] and was found to be not rate-dependent. During the primary stages of lithium deintercalation, phase transitions begin to display heterogeneity, and may stem from volume-change-induced stress. Clarification of rate-dependent phase transition mechanisms and particle cracking provides fundamental information about the lithium deintercalation process of electrode materials and suggests that the rational design of electrodes must accommodate heterogeneous phase changes in order to improve electrochemical performance.

4.2. X-ray Tomographic Microscopy

XTM is an X-ray microscopy technique based on the same principles as computed tomography (CT).[191] Similar to TXM, a collimated and coherent X-ray is transmitted through a sample that is rotated at various degrees to obtain the desired data. During sample rotation, a series of projected images will be collected that will reflect the total absorption of the sample in a specific orientation. Using a tomographic reconstruction algorithm, a 2D cross-sectional XTM image of the sample can be obtained. Furthermore, 3D spatial distribution images can be constructed using 2D XTM images of the sample. Moreover, as the attenuation of specific elements is highly related to photon energy, TXM is an element-sensitive technique that can be used to investigate the distribution of elements. Hence, the microstructural heterogeneity of electrode materials for LIBs can be probed via XTM.

The 3D microstructure of electrode materials and prepared electrodes have been studied using XTM.[27,192,193] In the case of $LiNi_{0.4}Mn_{0.4}Co_{0.2}O_2$, Lin et al. utilized XTM to elucidate the behavior of metal particle segregation, especially at the surface section of secondary particles. As nickel at the surface becomes depleted, secondary particles demonstrate performance associated with particles that are Ni-poor and Mn-rich. In addition to single electrode particles, the microstructure of electrodes prepared with graphite and NMC has also been investigated by XTM.[27,193] As for electrodes prepared using NMC and additives (i.e., binders and carbon black), XTM has been carried out to track the microstructure of the materials distribution and inside crack in electrode materials after pressing electrodes. The study of electrodes via XTM highlights the ability of this technique to probe the microstructure of materials at various length scales. This includes nanometer resolution for single particles and micrometer resolution for electrodes. Hence, microstructure variations in electrodes, including active particles and the porous nature between active particles, can be tracked via TXM to elucidate information regarding the route for electrochemical reactions.

Alloy-type anode materials for LIBs have attracted research attention, but many of these materials suffer from huge volume changes during the lithiation/delithiation process.[194] To improve the cyclability of these anode materials, there is an urgent need to investigate microstructural changes. Recently, morphological variations in Sn and Ge -based anode materials have been investigated using TXM. These studies have resulted in advancements in improving structural stability during cycling.[181,195,196] As shown in **Figure 14**, Ebner et al.[195] tracked the structural evolution of SnO as an anode material for LIBs during the lithiation process using TXM. By obtaining a set of 2D cross-section attenuation coefficient data along with 3D rendering images, revolution of the SnO particles during discharge process was attainable. As the attenuation coefficient is related to material composition, the lithiation mechanism was found to proceed via a core–shell process, undergoing conversion reactions and lithium alloying reactions. In addition, volume change-induced cracks have been investigated to tend to initiate and grow along the pre-existing defects. Afterward, the structure of materials would be damaged owing to the volume change was irreversible. In addition to SnO, Ge and Sn, as an anode material, have been investigated using TXM and display a similar volume change and crack formation behavior.[181,196] The huge volume change and induced cracks further pulverize the electrode material, resulting in rapid capacity fading. TXM provides high 3D spatial and time resolution and can be used

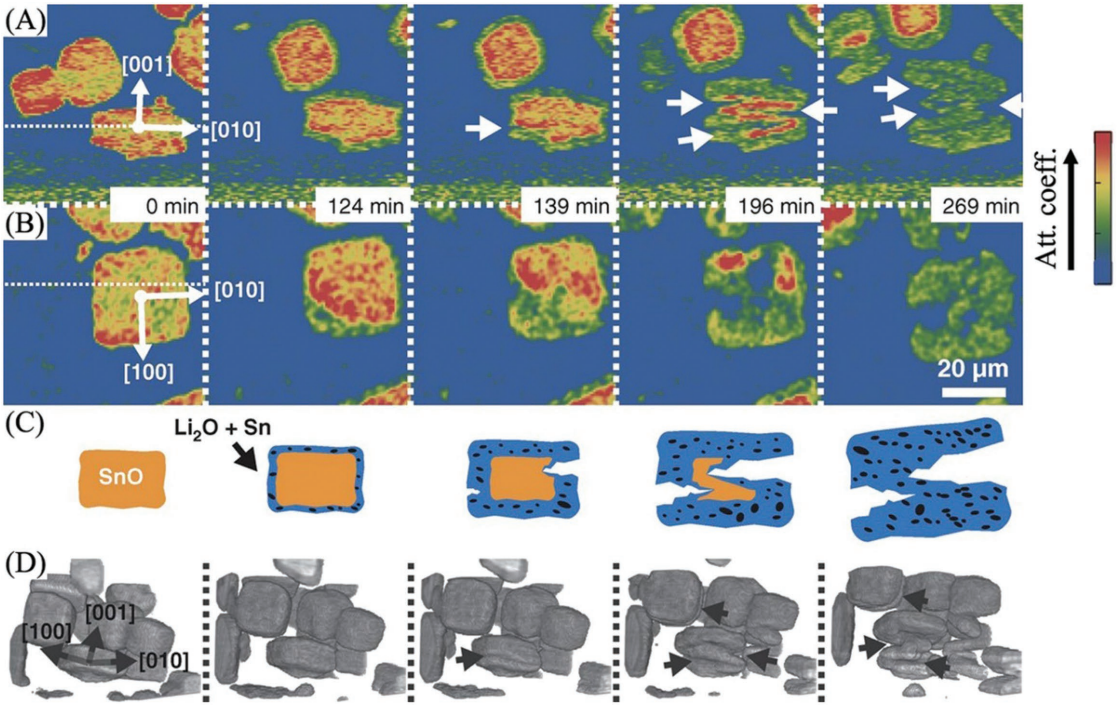

Figure 14. Morphology evolution of SnO particle. A) Coronal and B) transverse cross-section XTM images of a SnO particle during lithiation process. White arrows point to crack locations. C) Schematic illustration of particle phase evolution and crack growth leading to zigzag morphology. D) 3D rendering of subvolume visualizing zigzag morphology in multiple particles. Reproduced with permission.[195] Copyright 2013, American Association for the Advancement of Science.

to track chemical and morphological changes in electrode materials. The TXM investigation would make a great contribution to the comprehensive understanding of energy materials, improving advanced structure design to solve the capacity fading challenges.

5. Summary and Perspective

Here, we summarized the recent progress in the application of SR techniques for the study of lithium secondary batteries. Owing to the development of third generation SR sources, various techniques have been widely applied to investigate electrode and electrolyte materials. With a focus on XAFS, SXRD, and X-ray microscopy, measuring principles have been introduced to explain how these characterization techniques are employed in various research projects. The discussed characterization techniques can provide several types of resolution, including structural and chemical states, local environment, spatial and time resolution. In the case of structural and chemical investigation, the electronic structure, chemical environment, and crystal structure have been intensively investigated using XANES, EXAFS, and SXRD. The high sensitivity of the techniques makes a great contribution to probe the materials with coexistence phases, showing what elements, chemical states, crystal structures, and chemical environment exactly are involved. Additionally, structural and chemical states in different parts of bulk materials always display heterogeneous characteristics, which can be probed via the X-ray microscopy techniques, including TXM and XTM, showing high spatial resolution in 2D and 3D investigation. The combination of average and heterogeneous information is important to obtaining a comprehensive picture electrode and electrolyte materials. Furthermore, various characterization strategies, based on ex situ, in situ, and operando, have been highlighted and demonstrates the importance of time-resolution-based investigations. The electrochemical reaction, structural and chemical changes during battery operation determine the electrochemical performance, which plays a crucial role in the practical application of batteries. The characterization strategies performed by combining with the electrochemical process and other treatment (e.g., thermal abuse) provide an essential opportunity to track the electrochemical reaction and structural and chemical changes in real time. The characterization result with the several types of resolution is of vital significance to the comprehensive understanding of battery research. The new insights of reaction mechanism, electrode failure, and interface evolution would promote the advanced design and preparation of electrode and electrolyte materials.

Regarding the future direction for the application of SR techniques in next-generation high-energy lithium secondary batteries, the combination of various characterization techniques, and further improvement of resolution and development of new techniques are of great importance to battery development. First, the combination of different techniques has been already carried out to probe vast information (e.g., structure and composition) of materials simultaneously, such as TXM-XANES. The further combination of techniques with various characterization resolution, especially combining time resolution with others to real-time monitor materials could benefit the understanding and

development of batteries. Second, the resolution discussed above should be further improved to obtain more accurate and comprehensive information. As for the chemical states and local environment, higher spatial and energy resolution is required to not only realize qualitative analysis but also quantitative calculation. The more detailed quantitative investigation result can achieve the better understanding of unclear reaction mechanism. In addition to the improvement spatial and energy resolution of SR-based techniques, the time resolution should also be enhanced to meet the demand of better understanding of batteries cycled at high current densities, where rapid degradation and nonequilibrium reaction mechanism need further understanding.[197,198] As for the most in situ or operando studies, the current densities of tested batteries are always very low to increase the cycling time for measurement. Fast detectors and data acquisition systems for SR-based techniques should be further developed to realize quick measurement, such as microstrip silicon detectors.[199,200] Finally, the development of new techniques includes two factors. The first one is the modification in configuration of electrochemical cells for SR techniques, which should be suitable for characterization to get enough signal intensity (e.g., fluorescence and transmitted X-ray) and enable the same electrochemical reaction under normal operation conditions. The second one is related to the analysis of obtained data from several SR techniques, such as theoretical calculation of XANES, transformation from microscopy data to 2D and the 3D mapping. As the SR techniques display the powerful ability to probe and track states evolution in batteries and provide rational suggestions for modification of batteries, the future development of lithium secondary batteries can be accelerated via the involvement of SR techniques, thus contributing to the commercialization of next-generation high-energy lithium secondary batteries.

Acknowledgements

W.L. and M.L. contributed equally to this work. This work was funded by the Nature Sciences and Engineering Research Council of Canada (NSERC), the Canada Research Chair Program, the Canada Foundation for Innovation (CFI), the Ontario Research Fund, the Canada Light Source (CLS) at the University of Saskatchewan, and the University of Western Ontario. CLS was supported by CFI, NSERC, NRC, CHIR, and the University of Saskatchewan. T.W. acknowledged the Advanced Photon Source, an Office of Science User Facility operated for the U.S. Department of Energy (DOE) Office of Science by Argonne National Laboratory, supported by the U.S. DOE under Contract No. DE-AC02-06CH11357.

Conflict of Interest

The authors declare no conflict of interest.

Keywords

lithium secondary batteries, SXRD, synchrotron, XAFS, X-ray microscopy

Received: October 27, 2017
Revised: December 20, 2017
Published online:

[1] S. Solomon, G.-K. Plattner, R. Knutti, P. Friedlingstein, *Proc. Natl. Acad. Sci. USA* **2009**, *106*, 1704.
[2] G. J. Herbert, S. Iniyan, E. Sreevalsan, S. Rajapandian, *Renewable Sustainable Energy Rev.* **2007**, *11*, 1117.
[3] B. Parida, S. Iniyan, R. Goic, *Renewable Sustainable Energy Rev.* **2011**, *15*, 1625.
[4] M. A. Green, Y. Hishikawa, W. Warta, E. D. Dunlop, D. H. Levi, J. Hohl-Ebinger, A. W. Ho-Baillie, *Prog. Photovolt.: Res. Appl.* **2017**, *25*, 668.
[5] Y. Kumar, J. Ringenberg, S. S. Depuru, V. K. Devabhaktuni, J. W. Lee, E. Nikolaidis, B. Andersen, A. Afjeh, *Renewable Sustainable Energy Rev.* **2016**, *53*, 209.
[6] A. Yoshino, *Angew. Chem., Int. Ed.* **2012**, *51*, 5798.
[7] B. Scrosati, J. Garche, *J. Power Sources* **2010**, *195*, 2419.
[8] M. S. Whittingham, *Chem. Rev.* **2004**, *104*, 4271.
[9] J.-M. Tarascon, M. Armand, *Nature* **2001**, *414*, 359.
[10] L. F. Nazar, M. Cuisinier, Q. Pang, *MRS Bull.* **2014**, *39*, 436.
[11] G. Girishkumar, B. McCloskey, A. Luntz, S. Swanson, W. Wilcke, *J. Phys. Chem. Lett.* **2010**, *1*, 2193.
[12] Y. X. Yin, S. Xin, Y. G. Guo, L. J. Wan, *Angew. Chem., Int. Ed.* **2013**, *52*, 13186.
[13] J. W. Choi, D. Aurbach, *Nat. Rev. Mater.* **2016**, *1*, 16013.
[14] J. Lu, T. Wu, K. Amine, *Nat. Energy* **2017**, *2*, 17011.
[15] M. Wild, L. O'Neill, T. Zhang, R. Purkayastha, G. Minton, M. Marinescu, G. Offer, *Energy Environ. Sci.* **2015**, *8*, 3477.
[16] X. H. Liu, J. Y. Huang, *Energy Environ. Sci.* **2011**, *4*, 3844.
[17] R. Bhattacharyya, B. Key, H. Chen, A. S. Best, A. F. Hollenkamp, C. P. Grey, *Nat. Mater.* **2010**, *9*, 504.
[18] K. P. Yao, D. G. Kwabi, R. A. Quinlan, A. N. Mansour, A. Grimaud, Y.-L. Lee, Y.-C. Lu, Y. Shao-Horn, *J. Electrochem. Soc.* **2013**, *160*, A824.
[19] W. Huang, A. Marcelli, D. Xia, *Adv. Energy Mater.* **2017**, *7*, 1700460.
[20] S.-I. Nishimura, G. Kobayashi, K. Ohoyama, R. Kanno, M. Yashima, A. Yamada, *Nat. Mater.* **2008**, *7*, 707.
[21] S. Brutti, V. Gentili, H. Menard, B. Scrosati, P. G. Bruce, *Adv. Energy Mater.* **2012**, *2*, 322.
[22] C. Kunz, *J. Phys.: Condens. Matter* **2001**, *13*, 7499.
[23] F. Lin, Y. Liu, X. Yu, L. Cheng, A. Singer, O. G. Shpyrko, H. L. Xin, N. Tamura, C. Tian, T.-C. Weng, *Chem. Rev.* **2017**, *117*, 13123.
[24] D. H. Bilderback, P. Elleaume, E. Weckert, *J. Phys. B: At., Mol. Opt. Phys.* **2005**, *38*, S773.
[25] X. Liu, W. Yang, Z. Liu, *Adv. Mater.* **2014**, *26*, 7710.
[26] J. McBreen, *J. Solid State Electrochem.* **2009**, *13*, 1051.
[27] M. Ebner, F. Geldmacher, F. Marone, M. Stampanoni, V. Wood, *Adv. Energy Mater.* **2013**, *3*, 845.
[28] J. Nelson, S. Misra, Y. Yang, A. Jackson, Y. Liu, H. Wang, H. Dai, J. C. Andrews, Y. Cui, M. F. Toney, *J. Am. Chem. Soc.* **2012**, *134*, 6337.
[29] K. W. Nam, S. M. Bak, E. Hu, X. Yu, Y. Zhou, X. Wang, L. Wu, Y. Zhu, K. Y. Chung, X. Q. Yang, *Adv. Funct. Mater.* **2013**, *23*, 1047.
[30] X. Liu, T.-C. Weng, *MRS Bull.* **2016**, *41*, 466.
[31] X. Yu, Y. Lyu, L. Gu, H. Wu, S. M. Bak, Y. Zhou, K. Amine, S. N. Ehrlich, H. Li, K. W. Nam, *Adv. Energy Mater.* **2014**, *4*, 1300950.
[32] W.-S. Yoon, M. Balasubramanian, K. Y. Chung, X.-Q. Yang, J. McBreen, C. P. Grey, D. A. Fischer, *J. Am. Chem. Soc.* **2005**, *127*, 17479.
[33] J. Wang, Y.-C. K. Chen-Wiegart, J. Wang, *Nat. Commun.* **2014**, *5*, 4570.
[34] M. Balasubramanian, H. S. Lee, X. Sun, X.-Q. Yang, A. Moodenbaugh, J. McBreen, D. A. Fischer, Z. Fu, *Electrochem. Solid-State Lett.* **2002**, *5*, A22.
[35] K. Edström, M. Herstedt, D. P. Abraham, *J. Power Sources* **2006**, *153*, 380.
[36] M. Newville, *Rev. Mineral. Geochem.* **2014**, *78*, 33.

[37] B. H. Frazer, B. Gilbert, B. R. Sonderegger, G. De Stasio, *Surf. Sci.* **2003**, *537*, 161.
[38] M. Abbate, J. Goedkoop, F. De Groot, M. Grioni, J. Fuggle, S. Hofmann, H. Petersen, M. Sacchi, *Surf. Interface Anal.* **1992**, *18*, 65.
[39] J. Kawai, H. Adachi, S. Hayakawa, S. Y. Zhen, K. Kobayashi, Y. Gohshi, K. Maeda, Y. Kitajima, *Spectrochim. Acta, Part B* **1994**, *49*, 739.
[40] J. Stöhr, C. Noguera, T. Kendelewicz, *Phys. Rev. B* **1984**, *30*, 5571.
[41] A. Erbil, G. Cargill III, R. Frahm, R. Boehme, *Phys. Rev. B* **1988**, *37*, 2450.
[42] G.-L. Xu, T. Sheng, L. Chong, T. Ma, C.-J. Sun, X. Zuo, D.-J. Liu, Y. Ren, X. Zhang, Y. Liu, *Nano Lett.* **2017**, *17*, 953.
[43] J. Yano, V. K. Yachandra, *Photosynth. Res.* **2009**, *102*, 241.
[44] M. Shikano, H. Kobayashi, S. Koike, H. Sakaebe, Y. Saito, H. Hori, H. Kageyama, K. Tatsumi, *J. Power Sources* **2011**, *196*, 6881.
[45] Y. Piao, Y. Qin, Y. Ren, S. M. Heald, C. Sun, D. Zhou, B. J. Polzin, S. E. Trask, K. Amine, Y. Wei, *Phys. Chem. Chem. Phys.* **2014**, *16*, 3254.
[46] S. Yang, D. Wang, G. Liang, Y. M. Yiu, J. Wang, L. Liu, X. Sun, T.-K. Sham, *Energy Environ. Sci.* **2012**, *5*, 7007.
[47] T. Glaser, B. Hedman, K. O. Hodgson, E. I. Solomon, *Acc. Chem. Res.* **2000**, *33*, 859.
[48] Y. Tsai, J. Lee, D. Liu, B. Hwang, *J. Mater. Chem.* **2004**, *14*, 958.
[49] B. Ravel, M. Newville, *J. Synchrotron Radiat.* **2005**, *12*, 537.
[50] W.-S. Yoon, C. P. Grey, M. Balasubramanian, X.-Q. Yang, J. McBreen, *Chem. Mater.* **2003**, *15*, 3161.
[51] A. W. Brownrigg, G. Mountjoy, A. V. Chadwick, M. Alfredsson, W. Bras, J. Billaud, A. R. Armstrong, P. G. Bruce, R. Dominko, E. M. Kelder, *J. Mater. Chem. A* **2015**, *3*, 7314.
[52] B. Hwang, Y. Tsai, D. Carlier, G. Ceder, *Chem. Mater.* **2003**, *15*, 3676.
[53] B. Wang, J. Liu, M. N. Banis, Q. Sun, Y. Zhao, R. Li, T.-K. Sham, X. Sun, *ACS Appl. Mater. Interfaces* **2017**, *9*, 31786.
[54] B. Wang, J. Liu, Q. Sun, B. Xiao, R. Li, T. K. Sham, X. Sun, *Adv. Mater. Interfaces* **2016**, *3*, 1600369.
[55] H. Guo, X. Song, Z. Zhuo, J. Hu, T. Liu, Y. Duan, J. Zheng, Z. Chen, W. Yang, K. Amine, *Nano Lett.* **2015**, *16*, 601.
[56] J. Lu, Y. Qin, P. Du, X. Luo, T. Wu, Y. Ren, J. Wen, D. J. Miller, J. T. Miller, K. Amine, *RSC Adv.* **2013**, *3*, 8276.
[57] B. Xiao, B. Wang, J. Liu, K. Kaliyappan, Q. Sun, Y. Liu, G. Dadheech, M. P. Balogh, L. Yang, T.-K. Sham, *Nano Energy* **2017**, *34*, 120.
[58] J. Lu, C. Zhan, T. Wu, J. Wen, Y. Lei, A. J. Kropf, H. Wu, D. J. Miller, J. W. Elam, Y.-K. Sun, *Nat. Commun.* **2014**, *5*, 5693.
[59] J. Mao, K. Dai, M. Xuan, G. Shao, R. Qiao, W. Yang, V. S. Battaglia, G. Liu, *ACS Appl. Mater. Interfaces* **2016**, *8*, 9116.
[60] C.-Y. Chiang, H.-C. Su, P.-J. Wu, H.-J. Liu, C.-W. Hu, N. Sharma, V. K. Peterson, H.-W. Hsieh, Y.-F. Lin, W.-C. Chou, *J. Phys. Chem. C* **2012**, *116*, 24424.
[61] D. Wang, X. Li, J. Wang, J. Yang, D. Geng, R. Li, M. Cai, T.-K. Sham, X. Sun, *J. Phys. Chem. C* **2012**, *116*, 22149.
[62] D. Wang, X. Li, J. Yang, J. Wang, D. Geng, R. Li, M. Cai, T.-K. Sham, X. Sun, *Phys. Chem. Chem. Phys.* **2013**, *15*, 3535.
[63] D. Wang, J. Yang, X. Li, D. Geng, R. Li, M. Cai, T.-K. Sham, X. Sun, *Energy Environ. Sci.* **2013**, *6*, 2900.
[64] J. Yang, J. Wang, Y. Tang, D. Wang, X. Li, Y. Hu, R. Li, G. Liang, T.-K. Sham, X. Sun, *Energy Environ. Sci.* **2013**, *6*, 1521.
[65] P. Rozier, J. M. Tarascon, *J. Electrochem. Soc.* **2015**, *162*, A2490.
[66] P. He, H. Yu, H. Zhou, *J. Mater. Chem.* **2012**, *22*, 3680.
[67] R. Chen, W. Qu, X. Guo, L. Li, F. Wu, *Mater. Horiz.* **2016**, *3*, 487.
[68] D. Wang, L. Zuin, *J. Power Sources* **2017**, *337*, 100.
[69] A. Braun, H. Wang, J. Shim, S. S. Lee, E. J. Cairns, *J. Power Sources* **2007**, *170*, 173.
[70] J. Zhou, Y. Hu, X. Li, C. Wang, L. Zuin, *RSC Adv.* **2014**, *4*, 20226.
[71] X. Zhou, L. J. Wan, Y. G. Guo, *Adv. Mater.* **2013**, *25*, 2152.
[72] Y. Liu, L. Si, Y. Du, X. Zhou, Z. Dai, J. Bao, *J. Phys. Chem. C* **2015**, *119*, 27316.
[73] A. Frenkel, E. Stern, A. Voronel, M. Qian, M. Newville, *Phys. Rev. Lett.* **1993**, *71*, 3485.
[74] J. Mikkelsen Jr., J. Boyce, *Phys. Rev. B* **1983**, *28*, 7130.
[75] J. Boyce, J. Mikkelsen Jr., *Phys. Rev. B* **1985**, *31*, 6903.
[76] J. Bareno, M. Balasubramanian, S. Kang, J. Wen, C. Lei, S. Pol, I. Petrov, D. Abraham, *Chem. Mater.* **2011**, *23*, 2039.
[77] J. Rosolen, M. Abbate, *Solid State Ionics* **2001**, *139*, 83.
[78] Y. Terada, K. Yasaka, F. Nishikawa, T. Konishi, M. Yoshio, I. Nakai, *J. Solid State Chem.* **2001**, *156*, 286.
[79] P. Aitchison, B. Ammundsen, D. J. Jones, G. Burns, J. Rozière, *J. Mater. Chem.* **1999**, *9*, 3125.
[80] H. Kim, M. G. Kim, H. Y. Jeong, H. Nam, J. Cho, *Nano Lett.* **2015**, *15*, 2111.
[81] J. Lu, Y. Lei, K. C. Lau, X. Luo, P. Du, J. Wen, R. S. Assary, U. Das, D. J. Miller, J. W. Elam, *Nat. Commun.* **2013**, *4*, 2383.
[82] X. Li, Y. Xu, C. Wang, *J. Alloys Compd.* **2009**, *479*, 310.
[83] C. Ouyang, S. Shi, M. Lei, *J. Alloys Compd.* **2009**, *474*, 370.
[84] K. Amine, H. Tukamoto, H. Yasuda, Y. Fujita, *J. Electrochem. Soc.* **1996**, *143*, 1607.
[85] L. Li, L. Wang, X. Zhang, M. Xie, F. Wu, R. Chen, *ACS Appl. Mater. Interfaces* **2015**, *7*, 21939.
[86] H. Yamaguchi, A. Yamada, H. Uwe, *Phys. Rev. B* **1998**, *58*, 8.
[87] A. Iadecola, A. Perea, L. Aldon, G. Aquilanti, L. Stievano, *J. Phys. D: Appl. Phys.* **2017**, *50*, 144004.
[88] A. Rougier, C. Delmas, A. V. Chadwick, *Solid State Commun.* **1995**, *94*, 123.
[89] I. Nakai, K. Takahashi, Y. Shiraishi, T. Nakagome, F. Nishikawa, *J. Solid State Chem.* **1998**, *140*, 145.
[90] Y. K. Sun, Y. S. Jeon, H. J. Leeb, *Electrochem. Solid-State Lett.* **2000**, *3*, 7.
[91] Q. Qu, L. Fu, X. Zhan, D. Samuelis, J. Maier, L. Li, S. Tian, Z. Li, Y. Wu, *Energy Environ. Sci.* **2011**, *4*, 3985.
[92] H. Xia, Z. Luo, J. Xie, *Prog. Nat. Sci.: Mater. Int.* **2012**, *22*, 572.
[93] D. Song, H. Ikuta, T. Uchida, M. Wakihara, *Solid State Ionics* **1999**, *117*, 151.
[94] J. H. Yi, J. H. Kim, H. Y. Koo, Y. N. Ko, Y. C. Kang, J.-H. Lee, *J. Power Sources* **2011**, *196*, 2858.
[95] K. M. Shaju, P. G. Bruce, *Chem. Mater.* **2008**, *20*, 5557.
[96] Y. Tsai, B. Hwang, G. Ceder, H. Sheu, D. Liu, J. Lee, *Chem. Mater.* **2005**, *17*, 3191.
[97] J.-L. Shui, N. K. Karan, M. Balasubramanian, S.-Y. Li, D.-J. Liu, *J. Am. Chem. Soc.* **2012**, *134*, 16654.
[98] Y. Cui, A. Abouimrane, J. Lu, T. Bolin, Y. Ren, W. Weng, C. Sun, V. A. Maroni, S. M. Heald, K. Amine, *J. Am. Chem. Soc.* **2013**, *135*, 8047.
[99] M. Cuisinier, P.-E. Cabelguen, S. Evers, G. He, M. Kolbeck, A. Garsuch, T. Bolin, M. Balasubramanian, L. F. Nazar, *J. Phys. Chem. Lett.* **2013**, *4*, 3227.
[100] J. Wang, J. Yang, Y. Tang, R. Li, G. Liang, T.-K. Sham, X. Sun, *J. Mater. Chem. A* **2013**, *1*, 1579.
[101] R. Qiao, I. T. Lucas, A. Karim, J. Syzdek, X. Liu, W. Chen, K. Persson, R. Kostecki, W. Yang, *Adv. Mater. Interfaces* **2014**, *1*, 1300115.
[102] D. Takamatsu, Y. Koyama, Y. Orikasa, S. Mori, T. Nakatsutsumi, T. Hirano, H. Tanida, H. Arai, Y. Uchimoto, Z. Ogumi, *Angew. Chem., Int. Ed.* **2012**, *51*, 11597.
[103] H. Ota, T. Akai, H. Namita, S. Yamaguchi, M. Nomura, *J. Power Sources* **2003**, *119*, 567.
[104] S. Sallis, N. Pereira, P. Mukherjee, N. Quackenbush, N. Faenza, C. Schlueter, T.-L. Lee, W. Yang, F. Cosandey, G. Amatucci, *Appl. Phys. Lett.* **2016**, *108*, 263902.
[105] P. Harks, F. Mulder, P. Notten, *J. Power Sources* **2015**, *288*, 92.

[106] A. Deb, E. J. Cairns, *Fluid Phase Equilib.* **2006**, *241*, 4.
[107] M. Balasubramanian, X. Sun, X. Yang, J. McBreen, *J. Power Sources* **2001**, *92*, 1.
[108] L. Montoro, M. Abbate, J. Rosolen, *Electrochem. Solid-State Lett.* **2000**, *3*, 410.
[109] Y. Uchimoto, H. Sawada, T. Yao, *J. Synchrotron Radiat.* **2001**, *8*, 872.
[110] Y. Uchimoto, H. Sawada, T. Yao, *J. Power Sources* **2001**, *97*, 326.
[111] R. Qiao, L. A. Wray, J.-H. Kim, N. P. Pieczonka, S. J. Harris, W. Yang, *J. Phys. Chem. C* **2015**, *119*, 27228.
[112] Z. Zhuo, P. Olalde-Velasco, T. Chin, V. Battaglia, S. J. Harris, F. Pan, W. Yang, *Appl. Phys. Lett.* **2017**, *110*, 093902.
[113] W.-S. Yoon, K. Y. Chung, J. McBreen, K. Zaghib, X.-Q. Yang, *Electrochem. Solid-State Lett.* **2006**, *9*, A415.
[114] J. Leriche, S. Hamelet, J. Shu, M. Morcrette, C. Masquelier, G. Ouvrard, M. Zerrouki, P. Soudan, S. Belin, E. Elkaïm, *J. Electrochem. Soc.* **2010**, *157*, A606.
[115] X. Liu, D. Wang, G. Liu, V. Srinivasan, Z. Liu, Z. Hussain, W. Yang, *Nat. Commun.* **2013**, *4*, 2568.
[116] E. J. Crumlin, Z. Liu, H. Bluhm, W. Yang, J. Guo, Z. Hussain, *J. Electron Spectrosc. Relat. Phenom.* **2015**, *200*, 264.
[117] S. Hy, W.-N. Su, J.-M. Chen, B.-J. Hwang, *J. Phys. Chem. C* **2012**, *116*, 25242.
[118] W.-S. Yoon, K.-B. Kim, M.-G. Kim, M.-K. Lee, H.-J. Shin, J.-M. Lee, J.-S. Lee, C.-H. Yo, *J. Phys. Chem. B* **2002**, *106*, 2526.
[119] M. G. Kim, C. H. Yo, *J. Phys. Chem. B* **1999**, *103*, 6457.
[120] M. Katayama, K. Sumiwaka, R. Miyahara, H. Yamashige, H. Arai, Y. Uchimoto, T. Ohta, Y. Inada, Z. Ogumi, *J. Power Sources* **2014**, *269*, 994.
[121] K. Kirshenbaum, D. C. Bock, C.-Y. Lee, Z. Zhong, K. J. Takeuchi, A. C. Marschilok, E. S. Takeuchi, *Science* **2015**, *347*, 149.
[122] J. Liu, M. Kunz, K. Chen, N. Tamura, T. J. Richardson, *J. Phys. Chem. Lett.* **2010**, *1*, 2120.
[123] F. C. Strobridge, B. Orvananos, M. Croft, H.-C. Yu, R. Robert, H. Liu, Z. Zhong, T. Connolley, M. Drakopoulos, K. Thornton, *Chem. Mater.* **2015**, *27*, 2374.
[124] X. Liu, J. Liu, R. Qiao, Y. Yu, H. Li, L. Suo, Y.-S. Hu, Y.-D. Chuang, G. Shu, F. Chou, *J. Am. Chem. Soc.* **2012**, *134*, 13708.
[125] M. Balasubramanian, X. Sun, X. Yang, J. McBreen, *J. Electrochem. Soc.* **2000**, *147*, 2903.
[126] T. Nonaka, C. Okuda, Y. Seno, H. Nakano, K. Koumoto, Y. Ukyo, *J. Power Sources* **2006**, *162*, 1329.
[127] A. Manthiram, Y. Fu, S.-H. Chung, C. Zu, Y.-S. Su, *Chem. Rev.* **2014**, *114*, 11751.
[128] A. Manthiram, Y. Fu, Y.-S. Su, *Acc. Chem. Res.* **2012**, *46*, 1125.
[129] X. Li, A. Lushington, Q. Sun, W. Xiao, J. Liu, B. Wang, Y. Ye, K. Nie, Y. Hu, Q. Xiao, *Nano Lett.* **2016**, *16*, 3545.
[130] K. Y. Chung, W.-S. Yoon, K.-B. Kim, B.-W. Cho, X.-Q. Yang, *J. Appl. Electrochem.* **2011**, *41*, 1295.
[131] K. Yamamoto, T. Minato, S. Mori, D. Takamatsu, Y. Orikasa, H. Tanida, K. Nakanishi, H. Murayama, T. Masese, T. Mori, *J. Phys. Chem. C* **2014**, *118*, 9538.
[132] M. Wolf, B. M. May, J. Cabana, *Chem. Mater.* **2017**, *29*, 3347.
[133] Y. Oumellal, A. Rougier, G. Nazri, J. Tarascon, L. Aymard, *Nat. Mater.* **2008**, *7*, 916.
[134] A. K. Cheetham, A. P. Wilkinson, *Angew. Chem., Int. Ed.* **1992**, *31*, 1557.
[135] H. Cheng, C. Lu, J. Liu, Y. Yan, X. Han, H. Jin, Y. Wang, Y. Liu, C. Wu, *Prog. Nat. Sci.: Mater. Int.* **2017**, *27*, 66.
[136] M. Kunz, N. Tamura, K. Chen, A. A. MacDowell, R. S. Celestre, M. M. Church, S. Fakra, E. E. Domning, J. M. Glossinger, J. L. Kirschman, *Rev. Sci. Instrum.* **2009**, *80*, 035108.
[137] R. Robert, D. Zeng, A. Lanzirotti, P. Adamson, S. J. Clarke, C. P. Grey, *Chem. Mater.* **2012**, *24*, 2684.
[138] X. Zhang, M. Van Hulzen, D. P. Singh, A. Brownrigg, J. P. Wright, N. H. Van Dijk, M. Wagemaker, *Nat. Commun.* **2015**, *6*, 8333.
[139] E. S. Takeuchi, A. C. Marschilok, K. J. Takeuchi, A. Ignatov, Z. Zhong, M. Croft, *Energy Environ. Sci.* **2013**, *6*, 1465.
[140] K. C. Kirshenbaum, D. C. Bock, Z. Zhong, A. C. Marschilok, K. J. Takeuchi, E. S. Takeuchi, *J. Mater. Chem. A* **2015**, *3*, 18027.
[141] Y. Arachi, H. Kobayashi, S. Emura, Y. Nakata, M. Tanaka, T. Asai, H. Sakaebe, K. Tatsumi, H. Kageyama, *Solid State Ionics* **2005**, *176*, 895.
[142] M. Sathiya, A. M. Abakumov, D. Foix, G. Rousse, K. Ramesha, M. Saubanère, M. l Doublet, H. Vezin, C. Laisa, A. Prakash, *Nat. Mater.* **2015**, *14*, 230.
[143] H. Komatsu, H. Arai, Y. Koyama, K. Sato, T. Kato, R. Yoshida, H. Murayama, I. Takahashi, Y. Orikasa, K. Fukuda, *Adv. Energy Mater.* **2015**, *5*, 1500638.
[144] S. Mukerjee, T. Thurston, N. Jisrawi, X. Yang, J. McBreen, M. Daroux, X. Xing, *J. Electrochem. Soc.* **1998**, *145*, 466.
[145] X.-Q. Yang, X. Sun, J. McBreen, *Electrochem. Commun.* **2000**, *2*, 100.
[146] M. A. Lowe, J. Gao, H. D. Abruña, *J. Mater. Chem. A* **2013**, *1*, 2094.
[147] G. Parzych, D. Mikhailova, S. Oswald, J. Eckert, H. Ehrenberg, *J. Electrochem. Soc.* **2011**, *158*, A898.
[148] F. Wang, L. Wu, B. Key, X. Q. Yang, C. P. Grey, Y. Zhu, J. Graetz, *Adv. Energy Mater.* **2013**, *3*, 1324.
[149] A. Darwiche, C. Marino, M. T. Sougrati, B. Fraisse, L. Stievano, L. Monconduit, *J. Am. Chem. Soc.* **2012**, *134*, 20805.
[150] G. Tan, R. Xu, Z. Xing, Y. Yuan, J. Lu, J. Wen, C. Liu, L. Ma, C. Zhan, Q. Liu, *Nat. Energy* **2017**, *2*, 17090.
[151] Y. Cui, A. Abouimrane, C.-J. Sun, Y. Ren, K. Amine, *Chem. Commun.* **2014**, *50*, 5576.
[152] K. R. Ryan, L. Trahey, J. S. Okasinski, A. K. Burrell, B. J. Ingram, *J. Mater. Chem. A* **2013**, *1*, 6915.
[153] J.-L. Shui, J. S. Okasinski, P. Kenesei, H. A. Dobbs, D. Zhao, J. D. Almer, D.-J. Liu, *Nat. Commun.* **2013**, *4*, 2255.
[154] E. Knipping, C. Aucher, G. Guirado, F. Fauth, L. Aubouy, *New J. Chem.* **2017**, *41*, 7267.
[155] T. Thurston, N. Jisrawi, S. Mukerjee, X. Yang, J. McBreen, M. Daroux, X. Xing, *Appl. Phys. Lett.* **1996**, *69*, 194.
[156] S. Muhammad, H. Kim, Y. Kim, D. Kim, J. H. Song, J. Yoon, J.-H. Park, S.-J. Ahn, S.-H. Kang, M. M. Thackeray, *Nano Energy* **2016**, *21*, 172.
[157] A. M. Wise, C. Ban, J. N. Weker, S. Misra, A. S. Cavanagh, Z. Wu, Z. Li, M. S. Whittingham, K. Xu, S. M. George, *Chem. Mater.* **2015**, *27*, 6146.
[158] Q. Liu, G. Tan, P. Wang, S. C. Abeyweera, D. Zhang, Y. Rong, Y. A. Wu, J. Lu, C.-J. Sun, Y. Ren, *Nano Energy* **2017**, *36*, 197.
[159] Y. Orikasa, T. Maeda, Y. Koyama, H. Murayama, K. Fukuda, H. Tanida, H. Arai, E. Matsubara, Y. Uchimoto, Z. Ogumi, *Chem. Mater.* **2013**, *25*, 1032.
[160] H. Liu, F. C. Strobridge, O. J. Borkiewicz, K. M. Wiaderek, K. W. Chapman, P. J. Chupas, C. P. Grey, *Science* **2014**, *344*, 1252817.
[161] Y. Orikasa, T. Maeda, Y. Koyama, H. Murayama, K. Fukuda, H. Tanida, H. Arai, E. Matsubara, Y. Uchimoto, Z. Ogumi, *J. Am. Chem. Soc.* **2013**, *135*, 5497.
[162] M. Hess, T. Sasaki, C. Villevieille, P. Novák, *Nat. Commun.* **2015**, *6*, 8169.
[163] K.-N. Jung, J. Kim, Y. Yamauchi, M.-S. Park, J.-W. Lee, J. H. Kim, *J. Mater. Chem. A* **2016**, *4*, 14050.
[164] P. Balakrishnan, R. Ramesh, T. P. Kumar, *J. Power Sources* **2006**, *155*, 401.
[165] Q. Wang, P. Ping, X. Zhao, G. Chu, J. Sun, C. Chen, *J. Power Sources* **2012**, *208*, 210.

[166] B. Ravdel, K. Abraham, R. Gitzendanner, J. DiCarlo, B. Lucht, C. Campion, *J. Power Sources* **2003**, *119*, 805.
[167] M. Guilmard, L. Croguennec, D. Denux, C. Delmas, *Chem. Mater.* **2003**, *15*, 4476.
[168] M. Guilmard, L. Croguennec, C. Delmas, *Chem. Mater.* **2003**, *15*, 4484.
[169] Y. Baba, S. Okada, J.-I. Yamaki, *Solid State Ionics* **2002**, *148*, 311.
[170] Z. Chen, Y. Ren, E. Lee, C. Johnson, Y. Qin, K. Amine, *Adv. Energy Mater.* **2013**, *3*, 729.
[171] C.-k. Lin, Y. Piao, Y. Kan, J. Bareño, I. Bloom, Y. Ren, K. Amine, Z. Chen, *ACS Appl. Mater. Interfaces* **2014**, *6*, 12692.
[172] L. Cheng, W. Chen, M. Kunz, K. Persson, N. Tamura, G. Chen, M. Doeff, *ACS Appl. Mater. Interfaces* **2015**, *7*, 2073.
[173] E. Quartarone, P. Mustarelli, *Chem. Soc. Rev.* **2011**, *40*, 2525.
[174] C. Sun, J. Liu, Y. Gong, D. P. Wilkinson, J. Zhang, *Nano Energy* **2017**, *33*, 363.
[175] M. Tatsumisago, M. Nagao, A. Hayashi, *J. Asian Ceram. Soc.* **2013**, *1*, 17.
[176] J. C. Andrews, B. M. Weckhuysen, *ChemPhysChem* **2013**, *14*, 3655.
[177] A. Sakdinawat, D. Attwood, *Nat. Photonics* **2010**, *4*, 840.
[178] R. Falcone, C. Jacobsen, J. Kirz, S. Marchesini, D. Shapiro, J. Spence, *Contemp. Phys.* **2011**, *52*, 293.
[179] Y. Li, J. N. Weker, W. E. Gent, D. N. Mueller, J. Lim, D. A. Cogswell, T. Tyliszczak, W. C. Chueh, *Adv. Funct. Mater.* **2015**, *25*, 3677.
[180] J. Wang, Y.-C. K. Chen-Wiegart, J. Wang, *Chem. Commun.* **2013**, *49*, 6480.
[181] J. N. Weker, N. Liu, S. Misra, J. Andrews, Y. Cui, M. Toney, *Energy Environ. Sci.* **2014**, *7*, 2771.
[182] S.-C. Chao, Y.-C. Yen, Y.-F. Song, H.-S. Sheu, H.-C. Wu, N.-L. Wu, *J. Electrochem. Soc.* **2011**, *158*, A1335.
[183] U. Boesenberg, F. Meirer, Y. Liu, A. K. Shukla, R. Dell'Anna, T. Tyliszczak, G. Chen, J. C. Andrews, T. J. Richardson, R. Kostecki, *Chem. Mater.* **2013**, *25*, 1664.
[184] T. Warwick, H. Ade, S. Cerasari, J. Denlinger, K. Franck, A. Garcia, S. Hayakawa, A. Hitchcock, J. Kikuma, S. Klingler, *J. Synchrotron Radiat.* **1998**, *5*, 1090.
[185] F. Meirer, J. Cabana, Y. Liu, A. Mehta, J. C. Andrews, P. Pianetta, *J. Synchrotron Radiat.* **2011**, *18*, 773.
[186] J. N. Weker, Y. Li, R. Shanmugam, W. Lai, W. C. Chueh, *ChemElectroChem* **2015**, *2*, 1576.
[187] W. C. Chueh, F. El Gabaly, J. D. Sugar, N. C. Bartelt, A. H. McDaniel, K. R. Fenton, K. R. Zavadil, T. Tyliszczak, W. Lai, K. F. McCarty, *Nano Lett.* **2013**, *13*, 866.
[188] Y. Li, F. El Gabaly, T. R. Ferguson, R. B. Smith, N. C. Bartelt, J. D. Sugar, K. R. Fenton, D. A. Cogswell, A. Kilcoyne, T. Tyliszczak, *Nat. Mater.* **2014**, *13*, 1149.
[189] W. E. Gent, Y. Li, S. Ahn, J. Lim, Y. Liu, A. M. Wise, C. B. Gopal, D. N. Mueller, R. Davis, J. N. Weker, *Adv. Mater.* **2016**, *28*, 6631.
[190] Y. S. Yu, C. Kim, Y. Liu, A. Van Der Ven, Y. S. Meng, R. Kostecki, J. Cabana, *Adv. Energy Mater.* **2015**, *5*, 1402040.
[191] P. Pietsch, V. Wood, *Annu. Rev. Mater. Res.* **2017**, *47*, 451.
[192] F. Lin, D. Nordlund, Y. Li, M. K. Quan, L. Cheng, T.-C. Weng, Y. Liu, H. L. Xin, M. M. Doeff, *Nat. Energy* **2016**, *1*, 15004.
[193] P. Shearing, L. Howard, P. S. Jørgensen, N. Brandon, S. Harris, *Electrochem. Commun.* **2010**, *12*, 374.
[194] W. Li, X. Sun, Y. Yu, *Small Methods* **2017**, *1*, 1600037.
[195] M. Ebner, F. Marone, M. Stampanoni, V. Wood, *Science* **2013**, *342*, 716.
[196] J. Wang, Y.-C. K. Chen-Wiegart, J. Wang, *Angew. Chem., Int. Ed.* **2014**, *53*, 4460.
[197] J. Lim, Y. Li, D. H. Alsem, H. So, S. C. Lee, P. Bai, D. A. Cogswell, X. Liu, N. Jin, Y.-S. Yu, *Science* **2016**, *353*, 566.
[198] I. Takahashi, T. Mori, T. Yoshinari, Y. Orikasa, Y. Koyama, H. Murayama, K. Fukuda, M. Hatano, H. Arai, Y. Uchimoto, *J. Power Sources* **2016**, *309*, 122.
[199] V. Aulchenko, E. Pruuel, L. Shekhtman, K. Ten, B. Tolochko, V. Zhulanov, *Nucl. Instrum. Methods Phys. Res., Sect. A* **2017**, *845*, 169.
[200] U. Boesenberg, C. G. Ryan, R. Kirkham, D. P. Siddons, M. Alfeld, J. Garrevoet, T. Núñez, T. Claussen, T. Kracht, G. Falkenberg, *J. Synchrotron Radiat.* **2016**, *23*, 1550.